
Article:
Gong, P., Wynne, B.P., Knowles, A.J. et al. (4 more authors) (2020) Effect of ageing on the microstructural evolution in a new design of maraging steels with carbon. Acta Materialia, 196. pp. 101-121. ISSN 1359-6454

https://doi.org/10.1016/j.actamat.2020.06.029

Effect of ageing on the microstructural evolution in a new design of maraging steels with carbon

Peng Gong[a], Bradley P Wynne[a], Alexander J Knowles[b], Andrej Turk[c,d], Le Ma[a], Enrique I Galindo-Nava[c], W Mark Rainforth[a]*

[a]Department of Materials Science and Engineering, University of Sheffield, Sir Robert Hadfield Building, Mappin Street, Sheffield, S1 3JD, UK
[b]School of Metallurgy and Materials, University of Birmingham, Birmingham, B15 2TT, UK
[c]Department of Materials Science and Metallurgy, University of Cambridge, Cambridge, CB3 0F3, UK
[d]OxMet Technologies Ltd, Unit 15, Oxford Business Park, Yarnton, Kidlington, United Kingdom

Abstract

A new maraging steel, based on carbide precipitation, is described. Two alloys were designed namely Fe-10Mn-0.25C-2Cr-1Mo wt% (2CrMo) and Fe-10Mn-0.25C-1Cr-2Mo wt% (Cr2Mo). These compositions were chosen to achieve ultra-high strength and high tensile elongation; the former and latter are promoted through the simulatenous precipitation of Cr- and Mo-rich carbides and Mn-rich reverted austenite. The alloys were manufactured through the standard melting, casting and hot working route. Following a solution treatment at 870 °C and quench, which gave a fully martensitic structure, the alloys were aged for various times at 510 °C. The microstructure and tensile properties were investigated in detail as a function of ageing time. The microstructure observed was dominated by micron scale and nanometer scale Mn segregation which determined the local Ac_3 temperature. Austenite reversion occurred in both alloys, peaking at 16h in both cases. In the 2CrMo alloy, the reverted austenite was mainly globular in morphology due the Ac_3 temperature being lower than the ageing temperature, but was acicular in the Cr2Mo with Ac_3 similar to the ageing temperature of 510 °C. Moreover, acicular austenite was promoted by Mn segregation at martensite lath boundaries in Cr2Mo. In the 2CrMo steel, carbide precipitation (M_3C and M_7C_3) occurred during heating to the ageing

temperature, but the carbides gradually dissolved with further ageing. In contrast, in the Cr2Mo alloy, precipitation of carbides (M_7C_3 and M_2C) occurred during ageing, the volume fraction of which increased with ageing time. In both alloys a TRIP effect was observed, but the extent of this was greater for the Cr2Mo alloy. The complex microstructure obtained after 16h led to an excellent combination of strength of 1.3GPa and elongation of 18%. Physics-based models for the microstructure in martensite, precipitation kinetics, as well as for TRIP in austenite were employed to explain and predict the individual strengthtening contributions of the microstructure to the total strength, confirming that the maximum strength-elongation relationship found after 16h is due to an optimal combination of a slightly overaged - but still strong- martensite and 30% of reverted austenite, for increased work hardening and ductility.

Keywords: Medium Mn steel; austenite reversion; carbide precipitation; TRIP; Mn segregation/partioning.

*Corresponding author: m.rainforth@sheffield.ac.uk

1. Introduction

The development of inexpensive steel with an ultimate tensile strength above 1GPa and tensile elongations of 15-20% is a critical requirement in the automotive sector, particularly for light-weighting []-[3]. Initial high strength steels were nickel maraging steels developed in the late 1950s, based on the concept of using substitutional elements to produce age-hardening in a low-carbon iron-nickel martensitic matrix, with a high number density of fine intermetallic precipitates formed during ageing between 450°C and 500°C []-[13]. To reduce cost, Goldstein et al.[14] in 1960 used Mn as an alternative austenite stabilizer and reported excellent toughness obtained through a Transformation Induced Plasticity (TRIP) mechanism of austenite to

martensite []−[14]. This led to a significant level of research on Mn containing TRIP steels for enhanced levels of properties. More recently, maraging steels with no carbon and 9-15% Mn have been reported by Raabe and co-workers to exhibit an excellent ultimate tensile strength of 1-1.5 GPa with total tensile elongations of 15-20% []-[29]. These properties were attributed to precipitation of very fine nano-sized intermetallic compounds during the ageing heat treatment []-[32].

TRIP steels have been investigated extensively, which have a microstructure consisting of at least 5% of retained austenite embedded in hard phases like bainite, martensite and ferrite matrix [], []-[39]. During plastic deformation of a TRIP steel the austenite transforms to martensite, which markedly enhances the material properties and causes hardening. TRIP steels have a lower initial work hardening rate than Dual Phase (DP) steels, but the hardening rate persists at higher strains where work hardening of the DP begins to diminish []-[41].

In the current work, we report on a novel design approach for low cost, high ductility, high strength carbon-containing austenitic-martensitic steels. We have developed steels with an ultimate tensile strength up to 1.3 GPa and tensile elongation of 15-18% aided by carbide precipitation during heat treatment and the TRIP effect from the reverted austenite. Two steels are based on 10% Mn with minor additions of C, Cr and Mo to form nanoprecipitates. The main difference between the alloys is the Cr and Mo content. This gives a difference in the amount of reverted austenite they contain (an increase in the Cr content and decrease the Mo content results in an increase in the equilibrium transformation temperature between ferrite and austenite) and change in the kinetics of phase precipitation. This establishes a new way to design steels with excellent ultrahigh strength and ductility.

2. Alloy Design Rationale: Concealing the kinetics of fine-scale precipitation and austenite reversion

Maraging steels are a special class of carbon-free ultrahigh strength steels. These alloys comprise a lath martensitic matrix, stabilised by Ni and/or Co additions, and promote their strength from fine-scale precipitation of intermetallics. Although these steels display excellent combinations of very high-strength and toughness, whilst at the same time being easy to process requiring a single ageing step, the main two limitations in their widespread applications have been their very high costs and virtually no ductility at their peak-aged condition. For the former, it is possible to replace expensive additions of Ni and Co with ~10 wt% of Mn to stabilise lath martensite [42]. As for increasing the ductility, a viable solution has been to promote the reversion of (lath-shaped) austenite; we have shown that at least 30% of austenite is needed to increase the steel's ductility to ~20% [], [30]. Therefore, an ideal combination for superior strength (>1GPa) and elongation (>20%) is to promote fine-scale precipitation and 30% of austenite during ageing.

Such optimal microstructural combination is very difficult to achieve in intermetallic-forming steels; we have shown that times to reach peak hardness for typical intermetallics present in maraging steels, *e.g.* Ni_3Ti, NiAl, and Cu, are at least one order of magnitude shorter, 1h-100h, than the times required to form 30% of reverted austenite (>100h) when ageing between 450ºC-550ºC [42]. This conflicting issue demands for exploring other alloy compositions that can accelerate the kinetics of austenite and match it with fine precipitation.

If one looks at C-containing ultrahigh strength steels, such as Aermet 100 [43], AF1410 [44] and Ferrium C61 [45], they also contain a Ni/Co-rich martensitic matrix with the superior strength coming from the secondary hardening of Cr- and/or Mo-rich carbides, but they form very low amounts of reverted austenite [44]. Nonetheless, by adding Cr, Mo and C in Fe-10Mn we also expect that the reverted austenite will form much faster than C-free steels, since carbon

is an austenite-stabilising element and its diffusivity is at least one order of magnitude higher than Mn in α iron. Carbon content in these steels varies between 0.15-0.25 wt%, with higher strengths obtained with higher C contents.

The alloy composition is therefore defined as Fe-10Mn-0.25C-Cr-Mo to obtain a low cost, high ductility and high strength alloy. Two steel combinations are explored with different Cr and Mo additions (Fe-10Mn-0.25C-2Cr-Mo and Fe-10Mn-0.25C-Cr-2Mo), as we aim to interrogate what is the optimal Cr/Mo ratio for matching the kinetics of nanoprecipitation and austenite reversion. It is known that molybdenum aids in reducing phase growth kinetics [], [47]. The composition of the steels investigated in this study is listed in Table 1. Ageing at 510°C was chosen as an ideal compromise between high hardness and higher austenite kinetics, as reported in [], [44] for AF1410 and Aermet 100 having similar Cr and Mo additions.

Thermodynamic calculations were conducted using the Thermocalc TCFe8 database to anticipate the level of phase precipitation and solute partitioning. As for carbide selection, it has been reported in Fe-Cr-Mo-V-C that $M_{23}C_6$, M_3C and M_7C_3 are the phases more thermodynamically stable **Error! Reference source not found.**. The calculations include the phases BCC_A2, FCC_A1, Cementite, M_7C_3 and $M_{23}C_6$. Fig. 1 (a) and (b) show the thermodynamic predictions of the variations in phase fraction with temperature for 2CrMo and Cr2Mo, respectively. At 510°C for 2CrMo the volume fraction of $M_{23}C_6$ and M_7C_3 is 3.7% and 1%, respectively, whereas for Cr2Mo the fraction of $M_{23}C_6$ and M_7C_3 is dramatically inverted to 0.05% and 3.7%, respectively; no equilibrium M_3C was predicted in both cases. The equilibrium volume fraction of austenite for 2CrMo and Cr2Mo is predicted to be 38% and 35%, respectively; the austenite has a composition of 20 at% Mn and only ~ 0.24 at% of carbon. This composition corresponds to a stacking fault energy of 18 mJ m^{-2} [48], which suggests that the reverted austenite is not mechanically stable and shall undergo TRIP [49]. However, in multi-phase steels the transformation of reverted austenite into martensite is also influenced by

other factors such as austenite size and morphology, crystallographic orientation, neighbouring phases and defect density [36]. Provided that this is a gradual TRIP effect during tensile straining, the reverted austenite will increase the work hardening of the designed alloys.

2.1 Predicting the strength of multi-phase maraging steels

The variation in strength with ageing conditions in the designed alloys can be anticipated if the contribution of individual mechanisms to the total deformation in martensite and austenite are predicted, however these effects are complex and cannot be just simply added with a simple mixture rule. Instead, one can consider the iso-work principle stating that the mechanical work on the martensite and TRIP-ing austenite is equal, i.e. $\sigma_{\alpha\prime}\varepsilon_{\alpha\prime} = \sigma_{\gamma}\varepsilon_{\gamma}$, where σ_i and ε_i are the stress and strain induced on each phase, respectively. Following this idea, it is possible to estimate the linear strength of interacting phases in a two-phase steel [50]:

$$\sigma = \frac{V\sigma_{\gamma}\sqrt{\sigma_{\alpha\prime}}+(1-V)\sigma_{\alpha\prime}\sqrt{\sigma_{\gamma}}}{(1-V)\sqrt{\sigma_{\gamma}}+V\sqrt{\sigma_{\alpha\prime}}} \quad \text{Eq.1}$$

Where V is the volume fraction of austenite. Although this equation was derived for elastic deformation, it is useful to assess the relative contribution from the TRIP effect and from nanoprecipitiation in martensite.

$\sigma_{\alpha\prime}$ will depend on ageing time as: 1) the strength of the martensitic matrix σ_{matrix} changes due C diffusing to the forming precipitates and promoting dislocation recovery and 2) precipitation strengthening, σ_p, will vary according to the particle radius and volume fraction. The total strength of martensite can be written as:

$$\begin{aligned} \sigma_{\alpha\prime} &= \sigma_{matrix} + \sigma_p \\ \sigma_{matrix} &= \sigma_{ss} + \sigma_{GB} + \sigma_{dis} \end{aligned} \quad \text{Eq.2}$$

Where σ_{ss}, σ_{GB} and σ_{dis} are the solid solution strengthening, grain boundary strengthening and dislocation forest hardening terms, respectively, adding to the total strength in the matrix. Physics-based equations for σ_{ss}, σ_{GB} and σ_{dis} have been obtained in previous work in terms of steel's nominal composition, its prior austenite grain size -controlling the packet and block

size- and dislocation density – controlled by carbon additions; details of these expressions can be obtained from [51]. An important aspect to highlight in equation 2 is that the dislocation density depends strongly on the effective carbon content in the martensitic matrix as most carbon atoms segregate to dislocations, increasing their density with increasing carbon additions; however, carbon redistribution takes place during ageing and, to account for this effect, the effective carbon in the matrix x_{matrix} can be calculated from the mass balance equation: $x_C = x_{matrix}(1 - f_p) + \frac{1}{3} f_p$, where x_C is the nominal carbon content; this equation shows that the effective dislocation density decreases with increasing carbide volume fraction. The equation to estimate σ_p for needle-shaped particles, such as M_2C and M_7C_3, is given by [30]:$\sigma_p = \sqrt{\frac{a}{\pi}} 0.1 \mu b \frac{f_p^{1/2}}{r_p} \ln\left(\frac{r_p}{b}\right)$, where a is the particle aspect ratio and it has been measured to be ~3 for M_2C [52][53]; a similar ratio is assumed for M_7C_3. Precipitation kinetics needs to be considered to account for variations in σ_p during ageing. The Lifshitz-Slyozov-Wagner (LSW) equation for precipitate coarsening, along with the Johnson-Mehl-Avrami-Kolmogorov (JMAK) equation for the carbide volume fraction are used as a first approximation to avoid describing complex multi-component phase kinetics [30][54]:

$$r_p = \left(\frac{4}{9} K t\right)^{1/3}$$
$$f_p = f_{eq} \cdot \left(1 - \exp(-B t^n)\right) \qquad \text{Eq.3}$$

Where the LSW constant $K = 1.06 \times 10^{-30}$ m^3 s^{-1} was taken from[55]; this value was fitted for M_2C in AF1410 aged at 510 °C, a steel with similar Cr and Mo contents as Cr2Mo; the same value for K was assumed for M_7C_3 in 2CrMo, as no similar information was found in the literature. Similarly, B=0.456 and n=0.72 were fitted using data from [56] for the same steel. As for the equilibrium volume fraction, since M_2C was not predicted in the equilibrium calculations in Cr2Mo, this value is calculated using the lever rule, *i.e.* $f_{eq} = min(3 \cdot x_C, 3 \cdot x_{Mo}, 3 \cdot x_{Cr})$ where M=0.5Mo+0.5Cr was assumed. This gives $f_{eq} = 0.0305$.

As for σ_γ, we can estimate the maximum TRIP effect in the austenite using a model derived in previous work by one of the authors [46]. We assume a stacking fault energy of 18 mJ m^{-2} (previous Section) and set the equivalent strain in the austenite high enough such that it transforms completely (>90% strain). This is because the effective strain induced in the reverted austenite is complex to calculate when strain partitioning occurs at heterogeneous regions of martensite and austenite. The strength of (initially) reverted austenite after TRIP completes is 2282 MPa.

The combination of equations 2 and 3 allows us to predict the variation in strength of the martensitic matrix. This result combined with equation 1, can be used to determine the ageing time at which maximum strengthening will take place, if the volume fraction of reverted austenite is known. Due to the complex behaviour of austenite kinetics during ageing in these alloys, the volume fraction of reverted austenite will be taken from the measurements obtained in the following sections.

3. Experimental

3.1 Materials

The composition of the two steels investigated in this study is listed in Table 1, as evaluated by optical emission spectroscopy from AMG superalloys UK Limited. Both steels were produced as 12 mm diameter buttons with 8 mm thickness in an arc melting furnace with an argon atmosphere. The buttons were then homogenized at 1200 °C for 1 hour followed by quenching in oil to room temperature. The steels were then hot rolled at 1000 °C down to a thickness of 2 mm in two passes and oil quenched. Samples were austenitised at 870 °C for 1 hour and tempered at 510 °C for 5, 8, 16 and 48 hours followed by air-cooling. A schematic diagram showing the overall process route is given in Fig. 2. All heat treatments were undertaken in an Ar atmosphere in order to prevent oxidation and decarburization.

Table 1. Chemical compositions of the maraging steels (wt. %) taken from the sample on which the microstructural and mechanical characterisation was undertaken.

Materials	C	Si	Mn	Cr	Mo	P	S	Fe
Alloy 2CrMo	0.2	0.1	9.86	2.05	1.04	0.0016	0.005	Bal
Alloy Cr2Mo	0.22	0.09	9.51	0.95	1.9	0.0015	0.005	Bal

3.2 Tensile test

Tensile testing was also conducted for each processing condition at a constant strain rate of $10^{-4}s^{-1}$ using the sample geometry as shown in Fig. 3 at room temperature using a Zwick (BTC T1-FR020 TN A50) universal testing machine. Tensile tests were conducted three times for each condition.

3.3 Microstructure analysis

Microstructural observations were performed by optical microscopy (OM), scanning electron microscopy (SEM), electron backscatter diffraction (EBSD), and transmission electron microscopy (TEM). Specimens for OM, SEM and EBSD observation were prepared by standard metallographic methods, which included grinding from P400 to P1200 and polishing up to 0.04 µm colloidal silica particles. OM and SEM analyses were undertaken using a Nikon LV 150N and FEI-Nova 600, respectively using samples etched using a 2% nital solution for approximately 5-10s. The EBSD analyses were undertaken on a FEI-Nova 600 operating at 20 KV with a beam step size of 0.15-0.1µm. The HKL Channel 5 system (Oxford Instruments, Oxfordshire, United Kingdom) was used for data acquisition and analysis. The microstructure constituents in maraging steels can be distinguished by EBSD on the basis of following parameters: (1) the band contrast (BC) map depends on the distortions of the crystal lattice; (2) inverse pole figure map (IPF); (3) phase identification by analysing Kikuchi patterns. In order to have less error from the distortion in the crystals, 6 Kikuchi lines and 1.5 angular tolerances were employed to index the Kikuchi patterns to prevent misidentification.

Thin specimens for TEM were cut from the heat-treated blanks, and ground to about 60 μm using conventional techniques. The foils for TEM studies were prepared by both standard electropolishing and FIB lift-out techniques, with the later using a FEI-Helios dual-beam FIB. Elecropolishing was performed in a Tenupol Model twin-jet electropolishing unit, using a solution of 50 ml perchloric acid, 600 ml methanol and 350 ml butyl alcohol at a temperature of -40°C. FIB life-out was undertaken from specific sites to obtain the phase(s) of interest. TEM studies were conducted in a Philips 420 microscope operating at an accelerating voltage of 120 kV and a JEOL-F200 microscope operating at an accelerating voltage of 200 kV and a FEI Tecnai Osiris 80 operating at an accelerating voltage of 200 kV. The microstructural analyses were performed using both conventional diffraction contrast techniques with bright-field and dark-field images.

XRD measurements for phase analysis were performed on a Bruker D8 Advance diffractometer equipped with a Vantec position-sensitive detector and a graphite monochromator. Data was collected at room temperature using monochromatic Co Kα radiation (λ = 0.179026 nm), 45 kV, 35 mA, in the 2θ region between 30° and 135°. The step size is 0.034° (2θ) and the counting time per step is 10 seconds.

4. Results

4.1 Tensile tests

Tensile tests were undertaken on samples aged for 5h, 8h, 16h and 48h at 510 °C, Fig. 4. Table 2 summarises their tensile properties. A strong influence of the ageing time on the tensile curves was observed for both alloys. Ageing for 5 h gave a UTS of 949 MPa and 1114 MPa and elongations of 13.2 %, 9.4 % for 2CrMo and Cr2Mo respectively. As expected, a decrease in the tensile strength and elongation were observed after ageing for 8 h. The best mechanical properties for the two maraging steels was for 16h at 510 °C, which gave a UTS of 1024±26 MPa and elongation of 17.8±1.4 for the 2CrMo steel and a UTS of 1316±12 MPa and

elongations of 18.2±1.6 for the Cr2Mo alloy. Further ageing led to a decrease in the tensile strength and the elongation for both steels. The work-hardening rate curves are presented in Fig. 4 (c, d) for the samples aged for 5h and 16h. Both alloys aged for 16h had higher strain-hardening rate than the corresponding alloys with 5h aging over the entire loading range.

Table 2 Tensile test results of the two steels taken from 3 tests per condition

Steels	**Ageing Time (h)**	**Tensile Strength (MPa)**	**Elongation (%)**
2CrMo	5	949±21	13.2±2
	8	900±20	12±2.3
	16	1024±26	17.8±1.4
	48	748±15	4.6±1.0
Cr2Mo	5	1114±19	9.4±0.3
	8	1040±15	14.1±1.9
	16	1316±12	18.2±1.6
	48	1164±15	16.3±0.7

4.2 Microstructures after solution treatment and quench

Optical micrographs following austenitisation of 870 °C for 1h and oil quenching are shown in Fig. 5 (a-b). The microstructure was dominated by needle-like martensite. The XRD traces in Fig. 5 (c) show tetragonal and ε-martensite in both steels. The morphology of the martensite was similar in the two steels, and no peaks of austenite or carbides were detected.

4.3 Microstructures and mechanical properties after 510°C ageing with different times

4.3.1 Optical, SEM and XRD observations

Optical and SEM images of the two steels are given in Fig. 6 and Fig. 7. The optical microstructure appeared quite different after 5h ageing compared to the as-quenched state.

Some regions (lighter contrast) etched in a similar manner to the as-quenched state. However, there were also regions that etched rapidly and appeared dark in the optical micrographs. SEM showed that, after 5h etch, both the dark and light contrast regions were martensitic, but with a different etching response, Figs. 6 (e), 7 (e). The appearance of the microstructure was similar after the 8h ageing, although some regions did not etch at all, e.g. Fig. 7 (f). These regions appeared to be freshly formed tetragonal α´ martensite. After 16h ageing, there were distinct differences in the microstructural regions, Figs. 6 (f), 7 (f). Some regions had etched strongly, which were clearly tempered martensite, denoted α'_T. Some regions barely etched, although a lath structure could just be seen. These regions were freshly formed tetragonal α´ martensite, denoted fresh martensite, α'_F, as it formed during cooling from the ageing treatment. EDS of the two regions in the 2CrMo alloy, Fig. 6 (i, j) showed that the strongly etching region had significantly higher Mn than the lighter etching region. The Cr and Mo content was reproducibly slightly higher in the dark etching region. The same result was found for the Cr2Mo alloy, Fig. 7 (i, j).

XRD traces, Fig. 6 (i) and Fig. 7 (i), show that the extent of ε-martensite increased with ageing time, however the ε-martensite was not easily identifiable in the microstructure. XRD also showed that after ageing for 5h some reverted austenite had started to form. The reverted austenite increased significantly after ageing for 16 h, but then decreased for longer ageing times. Both alloys followed a similar trend, but Cr2Mo exhibited much more reverted austenite at 16 h than 2CrMo.

4.3.2 EBSD observations

For the as-quenched state, XRD traces show that if there was any reverted austenite, it was below detectable levels and therefore the microstructure to be composed entirely of martensite for both steels. Fig. 8 and 9 show EBSD inverse pole figure (IPF) maps, phase maps and band contrast (BC)) maps from alloy 2CrMo and alloy Cr2Mo, as a function of the annealing time

at 510 °C. For 5 h annealing at 510 °C, the phase maps show the microstructure to be composed entirely of martensite for both steels, Fig. 8 (a-c) and Fig. 9 (a-c). After annealing at 510 °C for 8 h, reverted austenite was observed, Fig. 8 (d-f) and Fig. 9 (d-f). The amount of reverted austenite was higher for 2CrMo than Cr2Mo after 8 h.

Increasing the annealing time to 16h increased the fraction of the austenite phase significantly in both steels, Fig. 8 (g-i) and Fig. 9 (g-i), but the amount of reverted austenite was much higher for Cr2Mo than 2CrMo. The morphology of the reverted austenite in the 2CrMo was different from that in the Cr2Mo. Following the definition used widely in the literature [56][57], two morphologies of reverted austenite were observed: acicular γ and globular γ. Acicular γ is nucleated at the martensite lath, block and packet boundaries, while globular γ is nucleated at prior γ boundaries as well as martensite block and packet boundaries. Fig. 8 shows IPF maps for alloy 2CrMo, showing that the globular γ was far more prevalent than the acicular form. Fig. 9 shows the orientation maps for alloy Cr2Mo. In this case, acicular γ was the dominant form (see e.g. Fig. 9 (e,f)). Because of the complexity of the austenite shapes, it was impossible to quantify the effective sizes of the austenite regions. However, the austenite was polycrystalline in all cases. An estimate of the grain size within the austenite was made using EBSD. The grain size within the globular regions in 2CrMo was quite small, 2.6±0.7 μm, shown in Fig. 8 (i), compared to acicular austenite in the Cr2Mo (8.1±0.6 μm) shown in Fig. 9 (i).

After increasing the annealing time to 48h, the austenite transformed back to fresh martensite (α'_F) on cooling from the ageing temperature in both alloys, the extent of which was greater for alloy Cr2Mo.

Fig. 10 shows the fraction of the reverted austenite as a function of ageing time measured from EBSD phase maps and by XRD. In most cases, there was little difference between the EBSD

and XRD values. The one exception to this was the for 2CrMo at 16h where XRD recorded a greater (23%) amount of austenite compared to the EBSD (16%). Of course, in XRD a much greater volume of material is sampled compared to EBSD. The differences did not alter the general trend. The amount of austenite increased up to a maximum at 16 h, and then decreased. Alloy Cr2Mo showed only a gradual increase in reverted austenite for 5 and 8 h, but then a rapid increase on going to 16 h age. In contrast, alloy 2CrMo showed a steady increase in reverted austenite up to the maximum at 16 h. The fraction of austenite was significantly higher in alloy Cr2Mo compared to alloy 2CrMo after 16 h ageing. For both alloys, ageing for 48 h gave a significant decrease in the amount of reverted austenite.

4.3.3 TEM observations of the microstructure

The formation of reverted austenite from the martensite as a function of ageing time was investigated by TEM. Mn segregation and the composition of the precipitated carbides was analysed by STEM-EDS to understand the role of elemental partitioning during ageing for times between 5 h and 48 h.

4.3.3.1 Alloy 2CrMo

Fig. 11 shows the microstructure of 2CrMo after ageing for 5 h, taken from the higher Mn region. The structure was predominantly tempered martensite, Fig. 11 (a) with some small fraction of reverted austenite in the martensite laths, Fig. 11 (b). The shape and featureless nature of the austenite suggested it is globular austenite. Carbide precipitation was extensive after ageing for 5 h on the lath martensite grain boundaries, as shown by the STEM-EDS Mn mapping Fig. 11 (c, d).

Fig. 12 shows alloy 2CrMo after ageing for 8h, showing the morphology of the reverted austenite. The selected area electron diffraction (SAED) pattern from Fig. 12 (a) indicated that

the martensite and reverted austenite has the Kurdjumov-Sachs (KR) orientation relationship (OR). The carbide number density was similar after 8h ageing, shown in Fig. 12 (c, d).

Fig. 13 (b) shows the morphology of the reverted austenite in the condition with the highest volume fraction of reverted austenite (16h), which still contained tempered martensite (α'_T) laths running through the austenite. There is a small rotation of 3° between the two parallel planes of $(111)_\gamma$ and $(110)_\alpha$. Interestingly, the extent of carbide precipitation was significantly less after ageing for 16h, as shown by the STEM EDS maps in Fig. 13 (c, d). After ageing for 48h, shown in Fig. 14 (a,b), there was extensive fresh twinned martensite present and the quantity of reverted austenite had reduced considerably. Moreover, at 48h, the carbides had disappeared and the composition appeared homogeneous, as shown by the STEM EDS maps Fig. 14 (c, d).

Carbide precipitation during the ageing process was complex. Fig. 11-14 (d) show the overall evolution of carbide formation and dissolution, while Fig. 15 shows a specific example after ageing 2CrMo for 8 h. Diffraction analysis indicated two types of carbides: M_3C (orthorhombic structure with a=0.451nm, b=0.508nm and c=0.672nm), (M=Cr, Fe, Mn) with the usual Bagaryatskii orientation to the martensitic matrix, which formed mainly within the martensite laths; and M_7C_3 (orthogonal structure with a=0.452nm, b=0.697nm, c=1.207nm), located on the martensite lath boundaries, Fig. 15 (b) and (c). Our observations are consistent with other authors reporting in Fe-Cr-Mo-C, with Cr/Mo ratio greater or equal than 1, the precipitation of predominantly M_3C and M_7C_3, over M_2C and $M_{23}C_6$ [47].

4.3.3.2 Alloy Cr2Mo

After ageing for 5h the early stages of formation of the acicular γ was observed on the martensite lath boundaries in alloy Cr2Mo, Fig. 16 (a, b), with no obvious precipitates in the tempered martensite, Fig. 16 (c, d). The SAED patterns from Figs. 16 after ageing for 5 h

indicated that the martensite and reverted austenite exhibited the Nishiyama-Wassermann (N-W) OR with $(111)_\gamma$ parallel to $(110)_\alpha$.

After ageing for 8h, the acicular γ had progressively grown along the martensite lath boundaries in alloy Cr2Mo Fig. 17 (a,b). The orientation relationship between reverted austenite and martensite remained the same as at 5h, namely, Nishiyama-Wassermann (N-W). A high residual dislocation density was also observed in the martensite adjacent to the reverted austenite. STEM EDS mapping indicated that Mn segregation was observed at most martensite lath boundaries, Fig. 17 (c, d), with no obvious precipitates on the boundaries. This is different to alloy 2CrMo where Mn segregation was not observed at martensite lath boundaries. Interestingly, Mn segregation was also observed at the austenite/martensite interfaces.

After ageing 16h, there were extensive regions of reverted austenite, Fig 18, with tempered martensite (α'_T) in it. The orientation relationship between austenite and martensite remained the same as that observed at 5 and 8 h ageing. Fresh martensite (α'_F) was also present (in Fig. 9 (h, i)), Fig. 18 (a, b). EDS Mn mapping showed that Mn segregation was still at the remaining martensite lath boundaries, and was also found at the austenite martensite boundaries, while the Mn was homogenously distributed in the reverted austenite phase, Fig. 18 (c, d).

After 48h the majority of the structure was martensite (α'_T and α'_F), Fig. 19, with larger precipitates formed on the grain boundaries and smaller precipitates formed inside of the grains Fig. 18 (b). The STEM images with corresponding EDS mapping images shown in Fig. 18 (c, d) that the reverted austenite transformed back to martensite.

The carbide evolution in Cr2Mo was significantly different to that in 2CrMo and is summarised in Fig. 16-19 (d). After 5h and 8h, the structure was mainly martensite with no carbide precipitation detected, Fig. 16 (c, d) and 17 (c, d) (in contrast to the 2CrMo alloy where extensive precipitation had occurred after 5h ageing, Fig. 11 (c) and (d)). Mn segregation was

detected within the reverted austenite, Fig. 15 (d). After ageing to 16h, carbide precipitation was observed throughout the structure, including in the reverted austenite. The extent of precipitation was even greater after 48h.

The morphology and crystallography of the carbides in alloy Cr2Mo is shown in Fig. 20 after annealing 16h at 510°C. The SAED pattern shows the OR relationship of $(010)\alpha//(01\bar{1}1)_{M2C}$ and $[100]\alpha//[2\,\overline{11}\,0]_{M2C}$ between the M_2C carbide and the martensitic matrix. The M_2C precipitates with hexagonal close-packed (hcp) structure (a=0.281nm, b=0.3nm, C=0.474nm), were located on the martensite lath boundaries and also inside the martensite. EDS indicated that the carbides were primarily Mo based, but with some Mn dissolved in them. Our findings are consistent with previous reports on the carbide precipitation sequence in Fe-Cr-Mo-C, with Cr/Mo ratio less than 1, where M_2C precipitation occurs preferentially over M_3C, M_7C_3 and $M_{23}C_6$ [58].

4.3.4 TRIP effect of the reverted austenite during tensile testing

Following tensile tests, all samples were examined by EBSD close to the region of failure, shown in Fig. 21 for both steels aged for 8h. For the 2CrMo steel there was 14.4% reverted austenite before the test. After the test there was 12.1 % austenite in the areas examined, Fig. 21 (a, b). The difference in austenite between before and after the test is probably within the statistical error; in any event, there was only a limited TRIP effect, if any. In the case of the Cr2Mo steel, the volume fraction of reverted austenite was less than 5% before the test, shown in Fig. 21 (c, d). After the test there was <1% austenite left, so a small TRIP effect had occurred.

After ageing for 16h, then most of the reverted austenite transformed during tensile testing for both alloys. Therefore, there was an extensive TRIP effect in both steels.

4.4 Modelling results

4.4.1 Comparing the measured and predicted carbide size and volume fraction

Figure 22 shows the predicted and measured a) average precipitate radius and b) volume fraction in 2CrMo and Cr2Mo. The average carbide radius was measured using thresholded TEM images in ImageJ; since this software assumed precipitates as circular, the radius of needle-shaped carbides was obtained by adding the correction factor $\frac{1}{\sqrt{a}}$ to the values calculated, i.e. identical areas were assumed between circular and cylindrical precipitates, the latter with length $a \cdot r_p$. For 2CrMo, no distinction between M_3C and M_7Cr_3 was considered due to the difficulties in isolating them experimentally. The measured average radii for 2CrMo were almost identical to those for Cr2Mo at all aging conditions; the predicted radius was smaller than those obtained experimentally only by up to ~1.5nm and it matched the experimental ones after 48h. As for the volume fraction, no $M_{23}C_6$ was identified in 2CrMo but M_7C_3 and M_3C were observed instead; therefore, the equilibrium volume fraction for M_7C_3 in this alloy was not considered in eq. 3, instead, the lever rule was used $f_{eq} = min\left(\frac{10}{3}x_C,\ \frac{10}{7}x_{Cr}\right) = 0.0308$. The modelling results in both steels are very similar, as f_{eq} is very similar; the model predictions were in good agreement with experiments with discrepancies of no more than ±0.01, except in 2CrMo at 48h and Cr2Mo at 5h. The discrepancy in 2CrMo at 48h can be due to the formation of reverted austenite which was not considered in the model; as for Cr2Mo, the difference could be due to more a sluggish nucleation process in M_2C, consistent with this steel having higher Mo [46], also not considered in the model. Improvements to model predictions can be done if the volume fraction and kinetics of individual carbides could be isolated. Nonetheless, an interesting aspect to highlight is that, irrespective of the carbide species forming or Cr+Mo combinations, it is apparent that precipitation coarsening is approximately the same in both steels.

4.4.2 Strength variations with ageing time

Tables 3 and 4 show the predicted strength and measured UTS (Table 2) for 2CrMo and Cr2Mo, respectively; the values for precipitation hardening, using the predicted values for f_p and r_p (Fig. 22), martensite strengthening and TRIP in the austenite are also shown for comparison, along with the relative contribution of (nanoprecipitation-strengthened) martensite and TRIP in the austenite using equation 1, *i.e.* including iso-work effects. The initial volume fraction of austenite was obtained from Fig. 10 considering results from EBSD. The predicted values of the strength in 2CrMo are in very good agreement with experiments, as they lie ±100MPa within the measured ones and the maximum strength is succesfully predicted to happen at 16h; the predicted UTS for Cr2Mo at 5h and 8h matches very well the measured ones, however the model predicts lower UTS at 16h and 48h, although again the model successfully predicts the maximum UTS at 16h. A reason for the discrepancy can be that the loss in martensite strength ($\sigma_{\alpha'}$), promoted by dislocation recovery**,** is not as pronounced as the model predicts.

As for the relative contribution to the total strength, although the TRIP-induced strength is very high in single-phase austenite (σ_γ), the TRIP contribution to the total strength is comparatively lower due to the much lower volume fraction of austenite. The TRIP contribution in 2CrMo is higher than Cr2Mo, except at the 16h condition, as the volume fraction of austenite in 2CrMo is higher. In addition, the predicted contribution of single-phase (nanoprecipitation-strenghtened) martensite is initially high in both steels but gradually decreases with ageing time. This is because σ_p decreases, as the predicted time to reach peak hardness is only ~1 h, but also σ_{matrix} decreases due to dislocation recovery and the loss in C content in the matrix promoted by carbide precipitation.

The maximum strength in Cr2Mo aged at 16 h is due to the increased TRIP effect from the higher austenite volume fraction (459 MPa), which in turn helps increasing the work hardening rate as experimentally observed in Fig. 4, as martensite contribution is lower at 16 h compared to other ageing times (728 MPa). This result validates our alloy design rationale, the maximum

strength and elongation obtained in Cr2Mo aged for 16h are due to an optimal combination of a slightly overaged, but still strong, martensite and 30% of reverted austenite, for increased work hardening and ductility.

Table 3. Predicted strengthening contributions in 2CrMo changing with ageing time.

Ageing time (h)	σ_p **(MPa)**	σ_{matrix} **(MPa)**	$\sigma_{\alpha'}$ **(MPa)**	σ_γ **(MPa)**	**Martensite contribution (MPa)**	**TRIP contribution (MPa)**	**Predicted Strength (MPa)**	**Strength Experiment (MPa)**
5	330	857	1187	2282	999	42	1041	949±21
8	325	762	1087	2282	841	198	1039	900±20
16	301	682	983	2282	750	225	975	1024±26
48	246	682	928	2282	751	116	867	748±15

Table 4. Predicted strengthening contributions in Cr2Mo changing with ageing time.

Ageing time (h)	σ_p **(MPa)**	σ_{matrix} **(MPa)**	$\sigma_{\alpha'}$ **(MPa)**	σ_γ **(MPa)**	**Martensite contribution (MPa)**	**TRIP contribution (MPa)**	**Predicted Strength (MPa)**	**Strength Experiment (MPa)**
5	329	948	1277	2282	1083	29	1112	1114±19
8	324	880	1204	2282	999	73	1072	1040±15
16	300	796	1096	2282	728	450	1178	1316±12
48	245	742	987	2282	821	66	887	1164±15

5. Discussion

5.1 Microstructural evolution in 2CrMo and Cr2Mo

After austenisation at 870°C for 1h, followed by water quenching, the structure of both alloys consisted entirely of martensite as shown by the XRD curves (Fig. 5). The Ac_3 temperature was calculated using Eq. 4 [59] for each steel, assuming the average alloy composition as shown in Table 1, which was found to be 538°C for alloy 2CrMo and 579°C for alloy Cr2Mo. This suggests that the selected aging temperature of 510°C was below the Ac_3 temperature in each case and therefore only tempering of the martensite would be expected. However, as discussed below, the local composition varied substantially from the average composition, such that some regions were above and some regions below the Ac_3 temperature.

$$Ac_3 = 910 - 203\sqrt{C} - 30Mn + 44.7Si - 11Cr + 31.5Mo \text{ -------- Eq. 4}$$

After ageing at 510°C for 5h, the microstructure of both alloys was separated into two differently etching regions, Fig. 6 and 7. These regions were investigated using EDS mapping in the SEM. The different etching response differentiated regions with distinctly higher Mn to those with lower Mn. The segregation of Mn meant that the Ac_3 temperature varied locally from one area to another. The local Ac_3 temperature was calculated from the EDS results and this is shown in Table 5. These calculations only give a broad idea as they do not account for where the C, Cr and Mo is, i.e. whether it remains in solution or has been removed through precipitation of carbides. Moreover, the calculations do not take into consideration the Mn segregated to the martensite lath boundaries. But the local Ac_3 estimations can be used as a proxy to differentiate local phase transition kinetics. The local changes in microstructure in the regions with higher Mn content were complex and must be understood in detail to understand the transformation behaviour.

Table 5. EDS measurements from the dark and light etching regions, shown in Figs. 6 and 7, with calculated A_{c3} temperatures

2CrMo					**Cr2Mo**				
Light / Ageing	Mn (wt%)	Cr (wt%)	Mo (wt%)	Ac_3 (°C)	Light / Ageing	Mn (wt%)	Cr (wt%)	Mo (wt%)	Ac_3 (°C)
5h	10.2	2	0.9	520	5h	9	0.9	2	563
8h	9.3	2	0.8	543	8h	9.2	0.8	2	555
16h	9.5	2.1	0.9	540	16h	9.4	0.9	1.6	551
48h	9.3	2	0.8	543	48h	9.4	0.9	1.8	548
Dark / Ageing	Mn (wt%)	Cr (wt%)	Mo (wt%)	Ac_3 (°C)	Dark / Ageing	Mn (wt%)	Cr (wt%)	Mo (wt%)	Ac_3 (°C)
5h	10.4	2	0.9	514	5h	10.2	0.9	2	527

8h	11.3	2	0.9	487	8h	10.8	1	2	508
16h	12.3	2.5	1.5	470	16h	11.9	0.9	2	495
48h	10.2	2.1	1	522	48h	9.8	0.9	1.7	542

5.1.1 The phase transformation mechanism in alloy 2CrMo

The Ac_3 temperature for the lower Mn region was higher than the ageing temperature, such that there was simple tempering of the martensite which had formed during the quench from solution treatment for all ageing times.

The situation in the high Mn regions was much more complex. The average composition of these regions is shown in Table 5, which indicates that the ageing temperature would have been generally above Ac_3 at the outset of ageing, which should have resulted in these regions reverting to austenite at the ageing temperature. However, only a small amount of reverted austenite was observed after 5h ageing as shown by XRD, Fig. 6, and TEM observations, Fig. 12. Fig. 6 (a, e), shows both fresh and tempered martensite indicating that some regions had indeed been above Ac_3. However, another factor must be considered. During the reheat to the ageing temperature significant carbide precipitation was observed on lath boundaries (primarily M_7C_3) and inside the laths (primarily M_3C), Fig. 11 (c, d). This precipitation removed C, Cr and Mo from solution and would have raised the Ac_3 temperature in the matrix by approximately 35 °C to well above the ageing temperature, thus reducing the amount of reverted austenite. The competition between carbide formation and austenite reversion has been studied in considerable detail by Kwiatkowski da Silva et al.[60] and shows that carbide formation leads to a delay in austenite reversion.

With an increase in ageing time to 8 h the carbides formed during the initial heating had started to dissolve. By 16h, the majority of prexisting M_7C_3 carbides had dissolved at the regions where

austenite has grown, Fig. 13 (c, d) and the austenite fraction was at a maximum. An approximate calculation of the dissolution temperature was made using Eq. 5, [18], using values of fc=1.02 and fcr=0.71 as obtained by [61].

$$\ln([wt\%Cr]^7[wt\%C]^3) = -417.6+356120/T-7\ln f_{Cr}-3\ln f_C \quad \text{Eq. 5}$$

This suggests a dissolution temperature of 550 °C, which is above the ageing temperature. However, there is clearly much uncertainty in this calculation given that the exact carbide composition was different.

The consequence of the dissolution of carbides was that the C, Cr, Mo in solution would have increased, therefore locally increasing the driving force for austenite reversion. The dissolution of carbides concurrent with the increase in volume fraction of reverted austenite is consistent with many observations, such as that of Lee and DeCooman [62] and Han and Lee [63]. Thus, the austenite reversion occurred through a diffusive reverse transformation leading to globular-shaped γ grains with a low dislocation density and a higher concentration of Mn than the martensite matrix, as observed by Han and Lee [63].

After aging to 48 h, the amount of reverted austenite at room temperature had decreased substantially, Figs. 8, 10. The microstructure, Figs. 8 and 14, contained a considerable amount of fresh martensite (α'_F) indicating that these regions were locally above Ac_3 during aging, with the reverted austenite had transformed to martensite on subsequent cooling. This was presumably because the reverted austenite had become large enough that it was sufficiently unstable to that it transformed to martensite on cooling.

5.1.2 The phase transformation mechanism in the alloy Cr2Mo

The behaviour of alloy Cr2Mo was quite different and the observation of a greater amount of reverted austenite was surprising given the alloy composition. The local compositions measured by EDS shown in Table 5 suggest that for most of the microstructure the ageing

temperature was below the Ac_3 temperature and therefore reverted austenite should not have been observed in the majority of the sample. However, as shown by Figs. 9 and 10, small amounts of reverted austenite were found after 5 h and 8 h and a considerable amount (~30%) after 16 h. The amount of reverted austenite was less in alloy Cr2Mo than in 2CrMo after 5 and 8 h age, but was greater after 16h, with about the same in both alloys after 48 h.

The morphology of the reverted austenite in alloy Cr2Mo was different to that in alloy 2CrMo. In alloy Cr2Mo, the reverted austenite was mainly acicular, forming along martensite lath boundaries, in contrast to the predominantly globular martensite in 2CrMo. This austenite obeyed the N-W orientation relationship with martensite (Figs. 17 and 18), namely: $(111)_{fcc}//(110)_{bcc}$, $[101]_{fcc}//[001]_{bcc}$. Acicular austenite forms at martensite lath boundaries, nucleating on the boundary and grows into one of the laths [64][65]. As Niessen [65] reported, when the ageing temperature is well above the Ac_3 temperature, then globular austenite is formed. In contrast, when the ageing temperature just above Ac_3, the acicular austenite is observed. Thus, these observations are consistent with the estimates of the Ac_3 temperature given in Table 5.

One important difference between the two alloys was the extent of Mn segregation at martensite lath, block and packet boundaries. Mn segregation was observed at most lath boundaries in alloy Cr2Mo, as shown in Figs. 17 and 18, but was not observed in 2CrMo. Mn segregation was also observed at the austenite/martensite interfaces. Segregation of Mn to martensite lath boundaries is commonly seen in medium Mn steels []-[71], and the origins of segregation to the austenite/martensite lath boundaries has been studied in detail by Dmitrieva et al. [20]. With the absence of precipitation at these boundaries, the local segregation of Mn on the boundaries was responsible for locally decreasing of Ac_3 temperature leading to the diffusionless reversion to austenite [63]. In contrast, in the 2CrMo steel, Mn segregation was rarely observed at the martensite lath boundaries. This was because of extensive precipitation

at lath boundaries that occurred during heating to the ageing temperature that was believed to locally remove the Mn into the precipitates (as shown in Figs. 11 (d)-13 (d)).

In Cr2Mo, the precipitation kinetics were considerably slower than 2CrMo (Figure 22(b)). The higher molybdenum content of Cr2Mo could have affected the phase transformation sequence by delaying the formation of M_2C, as reported in other steels [46][58], allowing for preferential Mn segregation and nucleation of austenite at the lath boundaries. Significant carbide formation was only observed after ageing for 16h in Cr2Mo, in contrast to 2CrMo, where carbide precipitation occurred on heating to the ageing temperature. However, to the authors knowledge, no other work has reported an influence of Mo in the kinetics for austenite reversion as a possible second-order effect.

After 48h, extensive precipitate formation had occurred, with a greater fraction than at earlier times. The solubility product of Mo_2C in austenite was computed by Eq. 3 with 1296°C [72].

$$\ln ([wt\%Mo][wt\%C]^{1/2})=3.04-2814/T \qquad \text{Eq. 3}$$

This is consistent with an increase in precipitate volume fraction with time, with M_2C (M=Mo, Mn) formed inside the reverted austenite (Fig. 18 (h) and (l)) and on martensite lath boundaries.

At 48h, the amount of reverted austenite observed in alloy Cr2Mo decreased, Fig. 10. The reason for the reduction was considered to be the same as for the 2CrMo alloy, namely that the reverted austenite had become large enough that, despite the Mn partitioning into it, it was sufficiently unstable to that it transformed to martensite on cooling. It is also because the removal of C and Mn by precipitation of the carbide would reduce the stability of the austenite.

The evolution of the microstructure as a function of ageing time is summarised in Fig. 23 for both alloys 2CrMo and Cr2Mo.

5.2 The effect of reverted austenite and carbides on the tensile strength

Fig. 3 shows the tensile mechanical properties as a function of heat treatment time. The behaviour of the two alloys was similar. The tensile strength decreased in going from 5h to 8h, with the decrease greater for Cr2Mo (~200MPa) compared to 2CrMo (~50MPa). The tensile strength showed a marked increase in going from 8h to 16h, giving the maximum value recorded for all heat treatment conditions. Finally, the tensile strength and the elongation to fracture decreased for those two alloys after ageing for 48h. In all cases, the elongation followed the same trend as the UTS, and more interestingly, the trends in elongation also are roughly consistent with the levels of reverted austenite before deformation. Our model sucessfully anticipated that the conditions giving maximum strength (16h) correspond to the cases for which the TRIP contribution is the highest, 225 MPa in 2CrMo and 450 MPa in Cr2Mo.

In going from 5h to 8h the drop in strength for the 2CrMo alloy was significant. The microstructural changes associated with this change were considerable. Firstly, the amount of reverted austenite increased significantly to 14.4%. However, little of this reverted austenite transformed on tensile testing, and so the TRIP effect would not have contributed to the strength or ductility. Our modelling results are consistent as only 73 MPa contribution from TRIP was predicted. Secondly, a significant fraction of fresh martensite was formed from regions that had been above Ac_3 and transformed to austenite, but then retransformed to martensite on cooling. These regions would have had an adverse effect on strength and ductility. Thirdly, extensive carbide precipitation had occurred on heating to the annealing temperature, but the amount of carbide had started to decrease in going from 5 to 8h.

Ageing for 16h led to an increase in strength and ductility to a level above that for 5h ageing, given the highest of both values for alloy 2CrMo. The principal changes in microstructure at 16h was a small change in the reverted austenite content and a further decrease in the carbides

content which continued to dissolve. These would not, in their own right, have led to an increase in strength and ductility, as correctly captured by the model in Table 4. However, the significant change was that the majority of the reverted austenite transformed during tensile deformation, which would have led to a significant change in both the strength and ductility. This was reflected in the change in work hardening behaviour, Fig. 4 (c). Further ageing to 48 h resulted in almost complete dissolution of the carbides, a reduction in the amount of reverted austenite and a significant coarsening of the structure, all of which would have led to the overall decrease in strength and ductility. Our model confirmed that samples aged for 48h had the lowest strength, although dissolution by austenite reversion was not considered; the low strength was due to a low martensite strength (only 751 MPa) due to extensive coarsening of carbides and a further reduction in austenite fraction had the TRIP contribution to be only 116 MPa.

For the Cr2Mo steel, then there was little (<5%) reverted austenite after 8h, and so only a minimal TRIP effect was observed (29 MPa). The Cr2Mo alloy also showed a drop in strength and ductility between 5h and 8h ageing, consistent with carbide coarsening (Table 4), but the extent of this was much less than for alloy 2CrMo. The changes in microstructure were similar to those for alloy 2CrMo, but with some important differences. Firstly, the amount of reverted austenite was very small and any TRIP effect would not have contributed significantly to strength and ductility, as predicted by the model, 29 MPa and 73MPa at 5h and 8h, respectively. Secondly, carbide precipitation was slowly developing in going from 5h to 8h. It is probable that the tempering of the martensite led to the observed reduction in strength. This was again captured by our model, where the strength of martensite (σ_{matrix}) dropped from 948 MPa to 880 MPa due to dislocation recovery.

The situation was quite different after ageing for 16h. This led to the maximum reverted austenite in the alloy Cr2Mo, the majority of which transformed during tensile deformation,

which has contributed significantly to the strength and ductility, as illustrated in Table 4. The TRIP effect was also reflected in the work hardening curves, Fig. 4d. Moreover, the carbide precipitation was extensive, both on the martensite lath boundaries and also inside the austenite, which will have contributed to the strength; the model predicted that, although the strength of martensite was lower at 16h, compared to 5h and 8h, it was still high enough (1096 MPa) to contribute considerably to the total strength. However, as with alloy 2CrMo, further ageing to 48h led to a coarsening of the structure and a reduction in the amount of austenite with no TRIP effect, resulting in a reduction in both strength and ductility. The model corroborated this effect by predicting that the TRIP contribution was only 66 MPa.

6. Conclusions

We designed two new maraging steels based on carbon precipitation, which exhibited excellent strength and ductility after ageing for 16h at 510°C steels. The kinetics of austenite reversion was much quicker than in equivalent carbon-free maraging steels. This new alloy design concept demonstrates that it is possible to conceal a key conflicting issue present in C-free maraging steels and in ultrahigh strength steels: promote simultaneous nano-precipitation, for high strength, and reversion of at least 30% of austenite, for high ductility. This was achieved by an optimal combination of Mn, Cr, Mo and C additions, which made the phase transformation behaviour interdependent but followed a complex sequence. The optimum microstructure comprised martensite with extensive carbide precipitation and reverted austenite. This reverted austenite exhibited an extensive TRIP effect which was important to obtaining the combination of high strength and ductility. Specific conclusions are:

1. Mn segregation occurred in both alloys. This led to some regions of the microstructure being aged above Ac_3, while other regions were below Ac_3. While this might be considered a negative outcome, it proved beneficial in developing the mechanical properties.

2. In the 2CrMo steel, carbide precipitation (M_3C and M_7C_3) occurred during heating to the ageing temperature. The precipitation of carbide appears to have prevented Mn segregation to the martensite lath boundaries. The carbides gradually dissolved during ageing until none were left after 48h at 510°C. Dissolution of carbides during ageing promoted local transformation to austenite. The carbides did not contribute strongly to the strength of the alloy.
3. The Mn rich regions in the 2CrMo alloy were aged well above the Ac_3 temperature, resulting the formation of globular reverted austenite. The maximum reverted austenite was observed for ageing for 16h, which provided the best combination of strength and ductility. This maximum in mechanical properties were produced by a structure comprising martensite, some carbides and reverted austenite that TRIPed on tensile testing.
4. For Cr2Mo steel, Mn segregation at the martensite lath boundaries led to the formation of acicular reverted austenite, nucleating on the martensite lath boundaries and subsequently growing into the laths. In contrast to 2CrMo, the carbides (M_2C) in the Cr2Mo steel formed did not form until it had been aged for 16 h. Thus, significant austenite reversion had occurred before carbide precipitation, demonstrating that an optimal Cr/Mo ratio of 0.5 aids in matching the (delayed) kinetics of carbide precipitation with (accelerated) austenite reversion.
5. The maximum strength and ductility was obtained for alloy Cr2Mo aged for 16h. This was associated with a microstructure comprising martensite, carbide precipitation on martensite lath boundaries and in the reverted austenite and the maximum content of reverted austenite. The reverted austenite completely transformed during the tensile test, such that the TRIP effect made a major contribution to strength and ductility.
6. Microstructure-sensitive models for the microstructure in martensite (dislocation and grain boundary density), precipitation kinetics, as well as for TRIP in austenite were

combined to predict and explain the individual strengthtening contributions of the microstructure to the total strength. Our model sucessfully anticipated that the conditions giving highest strength correspond to the cases for which the TRIP contribution is the highest, confirming that the maximum strength-elongation relationship found at 16h is due to an optimal combination of a slightly overaged - but still strong- martensite and ~30% of reverted austenite, for increased work hardening and ductility.

Acknowledgements

This work is supported by the EPSRC project "Designing Alloys for Resource Efficiency (DARE)", EP/L025213/1. E.I. Galindo-Nava would like to acknowledge the Royal Academy of Engineering for his research fellowship funding.

References

[1]. J. Milla´n, D. Raabe, P. Choi, O. Dmitrieva, Characterization of Nano-Sized Precipitates in a Mn-Based Lean Maraging Steel by Atom Probe Tomography, steel research int. 82 (2011) 137-145.
[2]. D. Raabe, D. Ponge, O. Dmitrieva, B. Sander, Nanoprecipitate-hardened 1.5 GPa steels with unexpected high ductility, Scr. Mater. 60 (2009) 1141-1144.
[3]. R. D. K. Misra, V.S.A. Challa, P.K.C. Venkatsurya, Y.F. Shen, M.C. Somani, L.P. Karjalainen, Interplay between grain structure, deformation mechanisms and austenite stability in phase-reversion-induced nanograined / ultrafine-grained austenitic ferrous alloy, Acta Mater. 84 (2014) 339-348.
[4]. B. B. He, B. Hu, H.W. Yen, G.J. Cheng, Z.K. Wang, H.W. Luo, M.X. Huang, High dislocation density-induced large ductility in deformed and partitioned steels, Science 357 (2017) 1029-1032.
[5]. Z. Zhang, M. Koyama, M.M. Wang, K. Tsuzaki, C.C. Tasan, H. Noguchi, Effects of lamella size and connectivity on fatigue crack resistance of TRIP-maraging steel, Int. J. Fatigue. 100 (2017) 176-186.
[6]. W. Sha, A. Ye, S. Malinov, E.A. Wilson, Microstructure and mechanical properties of low nickel maraging steel, Mater. Sci. Eng. 536 (2012) 129-135.
[7]. A. Kwiatkowski da Silva, G. Leyson, M. Kuzmina, D. Ponge, M. Herbig, S. Sandlobes, B. Gault, J. Neugebauer, D. Raabe, Confined chemical and structural states at dislocations in Fe-9wt % Mn steels: A correlative TEM-atom probe study combined with multiscale modelling, Acta Mater. 124 (2017) 305-315.
[8]. P. Kürnsteiner, M.B. Wilms, A. Weisheit, P. Barriobero-vila, A.J. Eric, Massive nanoprecipitation in an Fe-19Ni-xAl maraging steel triggered by the intrinsic heat treatment during laser metal deposition, Acta Mater. 129 (2017) 52-60.

[9]. E.A. Jägle, P. Choi, Precipitation and austenite reversion behavior of a maraging steel produced by selective laser melting, J. Mater. Res. 29(2014) 2072-2079.
[10]. N. H. Heo, H. C. Lee, Role of chromium on mechanical properties of Fe-Mn-Ni-Mo-Ti maraging steels, Met. Mater. 1 (1995) 77–83.
[11]. E. V Pereloma, A. Shekhter, M. K. Miller, S. P. Ringer, maraging alloy : clustering , precipitation and hardening, Acta Mater. 52 (2004) 5589-5602.
[12]. S. H. Nedjad, J. Teimouri, A. Tahmasebifar, H. Shirazi, M. N. Ahmadabadi, A new concept in further alloying of Fe-Ni-Mn maraging steels, Scr. Mater. 60 (2008) 528-531.
[13]. W. Xu, P.E.J. Rivera-Diaz-del-Castillo, W. Yan, K. Yang, D. San Martin, L.A.I. Kestens, S. van der Zwaag, A new ultrahigh-strength stainless steel strengthened by various coexisting nanoprecipitates, Acta Mater. 58 (2010) 4067-4075.
[14]. Ya. E. Goldshtein, G. A. Charushnikova, A. M. Belikov, Characteristic features of the phase transformations, structure, and properties of manganese steels, Izv. Akad. Nauk SSSR, Gornoe Delo, 4 (1963) 105-108.
[15]. J. Millan, S. Sandlo, A. Al-Zubi, T. Hickel, P. Choi, J. Neugebauer, D. Ponge, D. Raabe, Designing Heusler nanoprecipitates by elastic misfit stabilization in Fe-Mn maraging steels, Acta Mater. 76 (2014) 94-105.
[16]. C. Herrera, D. Ponge, D. Raabe, Design of a novel Mn-based 1GPa duplex stainless TRIP steel with 60% ductility by a reduction of austenite stability, Acta Mater. 59(11) (2011) 4653-4664.
[17]. L. Yuan, D. Ponge, J. Witting, P. Choi, J. A. Jimenez, D. Raabe, Nanoscale austenite reversion through partitioning , segregation and kinetic freezing: Example of a ductile 2 GPa Fe-Cr-C steel, Acta Mater. 60 (2012) 2790-2804.
[18]. O. Dmitrieva, D. Ponge, G. Inden, P. Choi, J. Sietsma, D. Raabe, Chemical gradients across phase boundaries between martensite and austenite in steel studied by atom probe tomography and simulation, Acta Mater. 59 (2010) 364-374.
[19]. S. Y. Li, X. J. Xi, Y. W. Luo, M. T. Mao, S. Xiao, J. Guo, H. J. Guo, Carbide precipitation during tempering and its effect on the wear loss of a high-carbon 8 Mass%Cr tool steel, Materials 11 (2018) 2491-2506.
[20]. B. D. Raabe, D. Ponge, O. Dmitrieva, B. Sander, Designing Ultrahigh Strength Steels with Good Ductility by Combining Transformation Induced Plasticity and Martensite Aging, Adv. Eng. Mater. (2009) 547-555.
[21]. Y. Toji, H. Matsuda, M. Herbig, P. Choi, D. Raabe, Atomic-scale analysis of carbon partitioning between martensite and austenite by atom probe tomography and correlative transmission electron microscopy, Acta Mater. 65 (2013) 215-228.
[22]. M. Calcagnotto, Y. Adachi, D. Ponge, D. Raabe, Deformation and fracture mechanisms in fine- and ultrafine-grained ferrite / martensite dual-phase steels and the effect of aging, Acta Mater. 59 (2010) 658-670.
[23]. D. Ponge, R. Song, M. Calcagnotto, D. Raabe, The formation of ultrafine grained microstructure in a plain C-Mn steel.
[24]. C. C. Tasan, M. Diehl, D. Yan, C. Zambaldi, P. Shanthraj, F. Roters, D. Raabe, Integrated experimental-simulation analysis of stress and strain partitioning in multiphase alloys, Acta Mater. 81 (2014) 386-400.
[25]. C. C. Tasan, J. P. M. Hoefnagels, M. Diehl, D. Yan, F. Roters, D. Raabe, Strain localization and damage in dual phase steels investigated by coupled in-situ deformation experiments and crystal plasticity simulations, Int. J. Plast. 63 (2014) 198-210.
[26]. C. Zheng, D. Raabe, Interaction between recrystallization and phase transformation during intercritical annealing in a cold-rolled dual-phase steel: A cellular automaton model, Acta Mater. 61 (2013) 5504-5517.
[27]. Ch. Ch. Eiselt, M. Klimenkov, R. Lindau, A. Möslang, H.R.Z. Sandim, A. F. Padilha, D. Raabe, High-resolution transmission electron microscopy and electron backscatter

diffraction in nanoscaled ferritic and ferritic-martensitic oxide dispersion strengthened-steels, J. Nucl. Mater. 385 (2009) 231-235.
[28]. R. Song, D. Ponge, R. Kaspar, D. Raabe, Grain boundary characterization and grain size measurement in an ultrafine-grained steel, Z. Metallkd. 95 (2004) 513-517.
[29]. R. Song, D. Ponge, D. Raabe, Mechanical properies of an ultrafine grained C-Mn steel processed by warm deformation and annealing, Acta Mater.53 (2005) 4881-4892.
[30]. E. I. Galindo-nava, W. M. Rainforth, P.E.J. Rivera-díaz-del-castillo, Predicting microstructure and strength of maraging steels : Elemental optimisation, Acta Mater. 117 (2016) 270-285.
[31]. M. N. Ahmadabadi, H. Shirazi, H. Ghasemi-nanesa, S. H. Nedjad, B. Poorganji, T. Furuhara, Role of severe plastic deformation on the formation of nanograins and nano-sized precipitates in Fe-Ni-Mn steel, Mater. Des. 32 (2011) 3526-3531.
[32]. T. Jialong, W. Wei, M. Babar Shahzad, Y. Wei, S. Yiyin, J. Zhouhua, Y. Ke, A New Maraging Stainless Steel with Excellent strength-toughness-corrosion synergy, Mater. (2017) 1293-1304.
[33]. J. Han, J.H. Nam, Y.K. Lee, The mechanism of hydrogen embrittlement in intercritically annealed medium Mn TRIP steel, Acta Mater. 113 (2016) 1-10.
[34]. J.K. Jung, O.Y. Lee, Y.K. Park, D.E. Kim, K.G. Jin, Hydrogen embrittlement behavior of high Mn TRIP/TWIP steels, Korean J. Mater. Res. 18 (2008) 394-399.
[35]. Z. Tang, J. Huang, H. Ding, Z. Cai, D. Zhang, D. Misra, Effect of deformation temperature on mechanical properties and deformation mechanisms of cold-rolled low C high mn TRIP/TWIP steel, Metals (Basel). 8 (2018) 476-487.
[36]. M. Wang, C. C. Tasan, D. Ponge, A. Kostka, D. Raabe, Smaller is less stable: Size effects on twinning vs. transformation of reverted austenite in TRIP-maraging steels, Acta Mater. 79 (2014) 268-281.
[37]. R. Schnitzer, G. A. Zickler, E. Lach, H. Clemens, S. Zinner, T. Lippmann, H. Leitner, Influence of reverted austenite on static and dynamic mechanical properties of a PH 13-8 Mo maraging steel, Mater. Sci. Eng. A. 527 (2010) 2065-2070.
[38]. W. Jeong, D. Matlock, G. Krauss, Effects of tensile-testing temperature on deformation and transformation behavior of retained austenite in a 0.14 C-1.2 Si-1.5 Mn steel with ferrite-bainite-austenite structure, Mater. Sci. Eng. A. 165 (1993) 9-18.
[39]. A. Kumar, S.B. Singh, K.K. Ray, Influence of bainite/martensite-content on the tensile properties of low carbon dual-phase steels, Mater. Sci. Eng. A. 474 (2008) 270-282.
[40]. J. Hu, L.X. Du, J. J. Wang, C. R. Gao, T. Z. Yang, A.Y. Wang, R.D.K. Misra, Microstructures and Mechanical Properties of a New As-Hot-Rolled High-Strength DP Steel Subjected to Different Cooling Schedules, Metall. Mater. Trans. A. 44 (2013) 4937-4947.
[41]. C. Y. Chen, C.C. Chen, J.R. Yang, Microstructure characterization of nanometer carbides heterogeneous precipitation in Ti-Nb and Ti-Nb-Mo steel, Mater. Charact. 88 (2014) 69-79.
[42]. A. J. Knowles, P. Gong, K. M. Rahman, W. M Rainforth, D. Dye, E. I. Galindo-Nava. Devel- opment of Ni-free Mn-stabilised maraging steels using Fe2SiTi precipitates. Acta Mater. 174 (2019) 260-27.
[43]. C. H. Yoo, H. M. Lee, J. W. Chan, J. W. Morris Jr. M_2C Precipitates in isothermal tempering of high Co-Ni secondary hardening steel, Metall. Mater. Trans. A 27 (1996) 3466-3472.
[44]. R. Ayer, P. M. Machmeier, Microstructural basis for the effect of chromium on the strength and toughness of AF1410-based high performance steels, Metall. Mater. Trans. A 27 (1996) 2510-2517.
[45]. J. Sebastian, J. Grabowski, D. Snyder, New high performance gear steels for rotorcraft transmission applications (Ferrium® C61™ and Ferrium C64™), ASME 2013 International

Design Engineering Technical Conferences and Computers and Information in Engineering Conference 5 (2013) V005T11A009.
[46]. S. Mukherjee, I. B. Timokhina, C. Zhu, S. P. Ringer, P. D. Hodgson. Three-dimensional atom probe microscopy study of interphase precipitation and nanoclusters in thermomechanically treated titanium–molybdenum steels. Acta Mater. 61 (2013) 2521-2530.
[47]. W. B. Lee, S. G. Hong, C. G. Park, K. H. Kim, S. H. Park. Influence of Mo on precipitiation hardening in hot rolled HSLA steels containing Nb. Scr. Mater. 43 (2000) 319-324.
[48]. D. T. Pierce, J.A. Jimenez, J. Bentley, D. Raabe , C. Oskay, J.E. Wittig. The influence of manganese content on the stacking fault and austenite/ε-martensite interfacial energies in Fe–Mn–(Al–Si) steels investigated by experiment and theory. Acta Mater. 68 (2014) 238–253.
[49]. E. I. Galindo-nava, P.E.J. Rivera-díaz-del-castillo, Understanding martensite and twin formation in austenitic steels: A model describing TRIP and TWIP effects , Acta Materilia 128 (2017) 120-134.
[50]. S. Lee, B.C. DeCooman, Influence of carbide precipitation and dissolution on the microstructure of ultra-fine-grained intercritically annealed medium manganese steel, Metal. Mater. Trans. A, 47A (2016) 3263-3270.
[51]. E. I. Galindo-Nava, P. E. J. Rivera-Díaz-del-Castillo, A model for the microstructure behaviour and strength evolution in lath martensite, Acta Materialia 98 (2015) 81-9.
[52]. R. Ayer, P.M. Machmeier, Transmission Electron Microscopy Examination of hardening and toughening phenomena in Aermet 100, Metallurgical Transactions 24A (1993) 1943-1955.
[53]. C. H. Yoo, H.M. Lee, J.W. Chan, J.W. Morris Jr, M2C precipitates in isothermal tempering of high Co-Ni secondary hardening steel, Metallurgical and Materials Transactions 27A (1996) 3466-3472
[54]. K. S. Cho, S.S. Park, H.K. Kim, Y.B. Song, H. Kwon, Precipitation Kinetics of M2C carbide in severly ausformed 13Co-8Ni secondary hardening steels, Metallurgical and Materials Transactions 46A (2915) 1535-1543
[55]. M. Grujicic, Design of M2C carbides for coarsening resistance, CALPHAD 15 (1991) 179-184
[56]. G. B. Olson, T.J. Kinkus, J.S. Montgomery, APFIM study of multicomponent M2C carbide precipitation in AF14010 steel, Surface Science 246 (1991) 238-245.
[57]. S. T. Kimmins, D. J. Gooch, Austenite memory effect in 1 Cr-1 Mo-0.75V (Ti , B) steel, Met. Sci. 17 (1983) 519-532.
[58]. X. Zhang, G. Miyamoto, Y. Toji, T. Furuhara, Effects of Heating Rate on Formation of Globular and Acicular Austenite during Reversion from Martensite, Metals (2019) 1-9 266-275.
[59]. R. J. Tunney, N. Ridley. Tempering of high-purity and commercially based steels containing 10 wt-% tungsten or 5 wt-% molybdenum, Metal Science 13:10 (1979) 585-590.
[60]. A. Kwiatkowski da Silva, G. Inden, A. Kumar, D. Ponge, B. Gault, D. Raabe, Competition between formation of carbides and reversed austenite during tempering of a medium-manganese steel studies by thermodynamic-kinetic simulations and atom probe tomography, Acta Mater. 147 (2018) 165-175.
[61]. K. W. Andrews. Empirical formulae for the calculation of some transformation temperatures, Journal of the Iron and Steel Institute, 203, part 7, 1965.
[62]. J. Han, Y-K Lee, The effects of the heating rate on the reverse transformation mechanism and the phse stability of reverted austenite in medium Mn steels, Acta Mater. 67 (2014) 354-361.
[63]. T. Koreaki, S. Jippei, Precipitation of carbides during temperaing of Cr Mo steels, Res. Rep. Fac. Eng. Mie Univ. 7 (1982) 39-52.

[64]. F. Niessen, Austenite reversion in low-carbon martensitic stainless steels-a CALPHAD-assisted review, J Mater. Sci. Tech. 34 (2018) 1401-1414.
[65]. Z. J. Xie, C. J. Shang, S. V. Subramanian, X. P. Ma, R. D. K. Misra, Atom probe tomography and numerical study of austenite stabilization in a low carbon low alloy steel processed by two-step intercritical heat treatment, Scr. Mater. 137 (2017) 36-40.
[66]. J. D. Escobar, J. D. Poplawsky, G. A. Faria, J. Rodriguez, J. P. Oliveira, C. A. F. Salvador, P. R. Mei, S. S. Babu, A. J. Ramirez, Compositional analysis on the reverted austenite and tempered martensite in a Ti-stabilized supermartensitic stainless steel : Segregation, partitioning and carbide precipitation, Mater. Des. 140 (2017) 95-105.
[67]. S. Sun, M. Pugh, Manganese partitioning in dual-phase steel during annealing, Mater. Sci. Eng. A. 276 (2000) 167-174.
[68]. Z. C. Li, H. Ding, R. D. K. Misra, Z. H. Cai, Microstructure-mechanical property relationship and austenite stability in medium-Mn TRIP steels: The effect of austenite-reverted transformation and quenching-tempering treatments, Mater. Sci. Eng. A. 682 (2016) 211-219.
[69]. I. R. S. Filho, A. Kwiatkowski, M. J. R. Sandim, D. Ponge, B. Gault, H. R. Z. Sandim, D. Raabe, Martensite to austenite reversion in a high-Mn steel: Partitioning-dependent two-stage kinetics revealed by atom probe tomography in-situ magnetic measurements and simulation, Acta Mater. 166 (2019) 178-191.
[70]. E. J. Pavlina, J. G. Speer, C. J. Van Tyne, Equilibrium solubility products of molybdenum carbide and tungsten carbide in iron, Scr. Mater. 66 (2011) 243-246.
[71]. W. Lee, S. Hong, C. Park, S. Park, Carbide precipitation and high-temperature strength of hot-rolled high-strength, low-alloy steels containing Nb and Mo, Metal. Mater. Tran. A 33 (2002) 1689-1698.
[72]. A. Ning, W. Mao, X. Chen, H. Guo, J. Guo, Precipitation Behavior of Carbides in H13 Hot Work Die Steel and Its Strengthening during Tempering, Metals 7(2017) 70-85.

Fig. 1. Equilibrum phase fraction variations with temperature predicted for (a) 2CrMo, (b) Cr2Mo.

Fig. 2. Schematic of the thermomechanical cycles applied to the alloys.

Fig. 3. Tensile sample geometry (lengths in mm).

Fig. 4. The tensile test curves as a function of the ageing time at 510 °C, (a) tensile curve from 2CrMo; (b) tensile curve from Cr2Mo; (c) work hardening rate curve from 2CrMo; (d) work hardening rate curve from Cr2Mo.

Fig. 5. Optical micrographs and XRD phase analysis of the two steels with austenitized treatment at 870 °C for 1h, (a) alloy 2CrMo; (b) alloy Cr2Mo; (c) XRD of the two steels.

Fig. 6. Micrographs of the maraging 2CrMo steel, etched in 2% nital. (a) OM at 510 °C for 5h; (b) OM at 510 °C for 8h; (c) OM at 510 °C for 16h; (d) OM at 510 °C for 48h; (e) SEM at 510 °C for 5h; (f) SEM at 510 °C for 8h; (g) SEM at 510°C for 16h; (h) SEM at 510 °C for 48h; (i) EDS spectrum from region labelled (i) from the α'_F in (g). Note carbon level is artificially high through carbon contamination; (j) EDS spectrum from region labelled (j) from the α'_T in (g). Note carbon level is artificially high through carbon contamination; (k) XRD for different heat treatment times for 2CrMo.

Fig. 7. Micrographs of the Cr2Mo steel, etched in 2% nital. (a) OM at 510 °C for 5h; (b) OM at 510 °C for 8h; (c) OM at 510 °C for 16h; (d) OM at 510 °C for 48h; (e) SEM at 510 °C for 5h; (f) SEM at 510 °C for 8h; (g) SEM at 510°C for 16h; (h) SEM at 510 °C for 48h; (i) EDS spectrum from region labelled (i) from α'_F in (g). Note carbon level is artificially high through carbon contamination; (j) EDS spectrum from region labelled (j) from α'_T in (g). Note carbon level is artificially high through carbon contamination; (k) XRD for different heat treatment times for 2CrMo.

Fig. 8. EBSD maps of 2CrMo showing the aged microstructure evolution from (a-c) 510 °C for 5h; (d-f) 510 °C for 8h; (g-i) 510 °C for 16h; (j-l) 510 °C for 48h. Inverse pole figures (IPF) maps (a,d,g,j) show the grain orientations with respect to RD (rolling direction); (b,e,h,k) phase maps with blue for FCC reverted austenite and red for martensite; (c,f,i,l) Band Contrast maps showing the morphology of the two phases..

Fig. 9. EBSD maps of Cr2Mo showing the aged microstructure evolution from (a-c) 510 °C for 5h; (d-f) 510 °C for 8h; (g-i) 510 °C for 16h; (j-l) 510 °C for 48h. Inverse pole figures (IPF) maps (a,d,g,j) show the grain orientations with respect to RD (rolling direction); (b,e,h,k) phase maps with blue for FCC reverted austenite and red for martensite; (c,f,i,l) Band Contrast maps showing the morphology of the two phases.

Fig. 10. The volume fraction of austenite in 2CrMo and Cr2Mo. The data from EBSD results with the specimens were annealed 5h, 8h, 16h and 48h at 510°C; the data from XRD results with the specimens were annealed 5h, 16h and 48h at 510°C.

Fig. 11. TEM and STEM micrographs on the 2CrMo after ageing for 5h: (a) STEM dark field image of two types of martensite (α'_T and α'_F) with carbides in the α'_T; (b) TEM image of reverted austenite in the martensite with corresponding select area electron diffraction (SAED) pattern. The reverted austenite has a mid-grey contrast and is featureless, suggesting it is globular austenite; (c) STEM high angle annular dark field image showing the tempered martensite with nanoscale carbides (d) corresponding EDS map showing the Mn distribution on lath martensite region from (c).

Fig. 12. TEM and STEM micrographs taken from 2CrMo after ageing for 8h: (a) TEM bright field image of reverted austenite in α'_T martensite phase with the corresponding SAED pattern; (b) TEM dark field image with $g=(011)_\alpha//(011)_\gamma$ from (a) shown the reverted austenite formed on the lath martensite boundaries; (c) STEM-dark field image in the α'_T martensite showing carbides and some reverted austenite particles on the lath grain boundaries and (d) STEM-EDS Mn map showing the carbides in (c).

Fig. 13. TEM and STEM micrographs taken from 2CrMo after ageing for 16 h: (a) TEM bright field image of reverted austenite in α'_T martensite phase with the corresponding SAED pattern; (b) TEM dark field image with g=$(011)_\gamma$ from (a) shown the reverted austenite; (c) STEM-dark field image of the austenite and tempered martensite and (d) EDS Mn map shown the carbides in corresponding image (c).

Fig. 14. STEM micrographs taken from 2CrMo after ageing for 48 h: (a) the STEM bright field image of tempered martensite (α'_T) and fresh martensite (α'_F); (b) higher magnification from the region marked in the red square showing the reverted austenite with partially transformed to fresh twinned martensite; (c) STEM-dark field image of fresh martensite, α'_F and (d) STEM EDS Mn mapping corresponding to image (c).

Fig. 15. Micrographs of carbide precipitates in 2CrMo steel after ageing for 8h: (a) the bright field image with its corresponding SAED pattern; (b) the dark field image of M_3C carbides takes with g=$(2\bar{1}\bar{1})_{M3C}$ from (a); (c) dark field of carbides taken with g=$(001\bar{1})_{M7C3}$ from (a).

Figure 16. TEM and STEM micrographs taken from Cr2Mo after ageing for 5h: (a) TEM bright field image from α'_T martensite with corresponding SAED pattern; (b) TEM dark field with g=$(011)_\gamma$ from (a) shown the reverted austenite sited on the martenite lath boundaries; (c) STEM-dark field image from α'_S martensite; (d) STEM EDS Mn map corresponding to image (c).

Figure 17. TEM and STEM micrographs taken from Cr2Mo after ageing for 8 h: (a) TEM bright field image from α'_T martensite with corresponding SAED pattern; (b) TEM dark field with g=$(011)_\gamma$ from (a) showing the reverted austenite growth along the martenite lath boundaries; (c) STEM-dark field image from α'_T martensite phase with martensite boundaries; (d) STEM EDS Mn mapping corresponding to image (c) showing Mn segregation with no carbides on the boundaries.

Fig. 18. TEM and STEM micrographs taken from Cr2Mo after ageing for 16 h: (a) TEM bright field image with corresponding SAED pattern from α'_T martensite and reverted austenite; (b) TEM dark field with g=$(011)_\gamma$ from (a) showing the reverted austenite; (c) STEM-bright field image from α'_T martensite with partially transformed to reverted austenite; (d) STEM EDS Mn mapping corresponding to image (c) showing carbides and Mn segregation at the austenite/martensite phase boundaries region and homogenous composition in the reverted austenite phase region.

Fig. 19. TEM and STEM micrographs taken from Cr2Mo after ageing for 48 h: (a) TEM bright field image of fresh martensite with its corresponding SAED pattern; (b) TEM dark field image with g=$(\bar{1}2\bar{1}0)_{M2C}$ from (a) showing large carbides on the grain boundaries and small carbides within the grains; (c) STEM-bright field image from fresh martensite; (d) STEM EDS Mn map corresponding to image (c) showing carbides formed in the region.

Fig. 20. Carbide precipitation in the tempered martensite in Cr2Mo aged for 16 hours. (a) TEM bright field image with its corresponding SAED pattern; (b) TEM dark field image of M_2C precipitates taken with g=$(0\overline{11}0)_{M2C}$ from (a) diffraction pattern; (c) TEM dark field of M_2C precipitates in the grains taken with g=$(000\bar{2})_{M2C}$ from (a) diffraction pattern.

Fig. 21. EBSD maps of the specimens aged for 8h (a-d) and 16h (a-d) after tensile testing: (a, b) 2CrMo showing some austenite retention after the tensile test; (c, d) Cr2Mo showing virtually no austenite after the tensile test; (e, f) 2CrMo showing virtually no austenite after the tensile test; (g, h) Cr2Mo showing virtually no austenite after the tensile test. (a, c) are IPF map and (b, c) are phase maps. (IPF: inverse pole figure; phase map: blue-reverted austenite, red-martenite).

Fig. 22. Predicted and measured carbide (a) effective radius and (b) volume fraction in 2CrMo and Cr2Mo.

Fig. 23. Schematic of the microstructural evolution, showing carbide precipitation, Mn segregation and the location and morphology of the reverted austenite for the two steels.

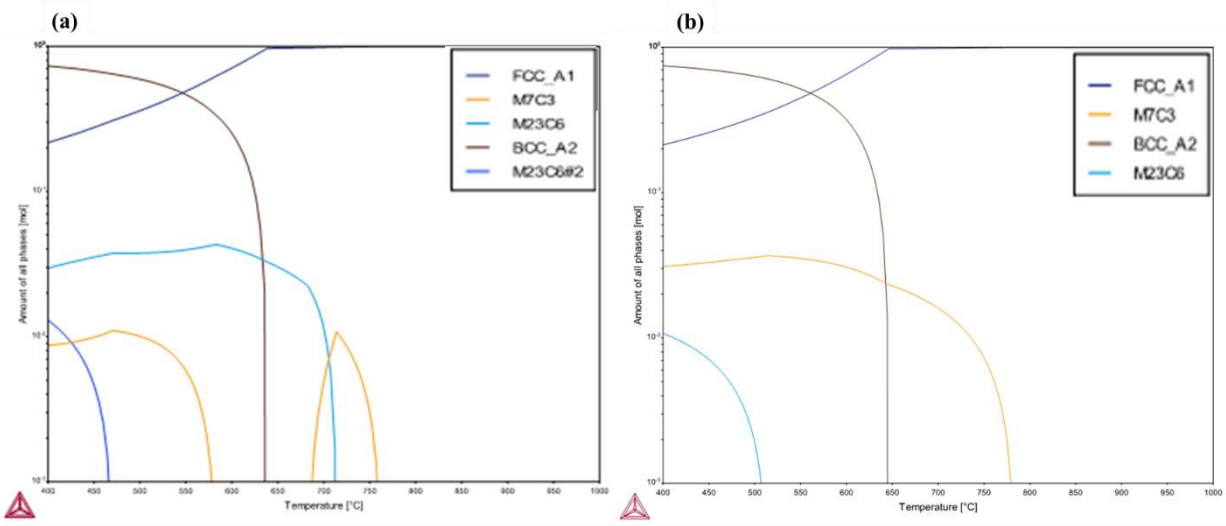

Fig. 1. Equilibrium phase fraction variations with temperature predicted for (a) 2CrMo, (b) Cr2Mo.

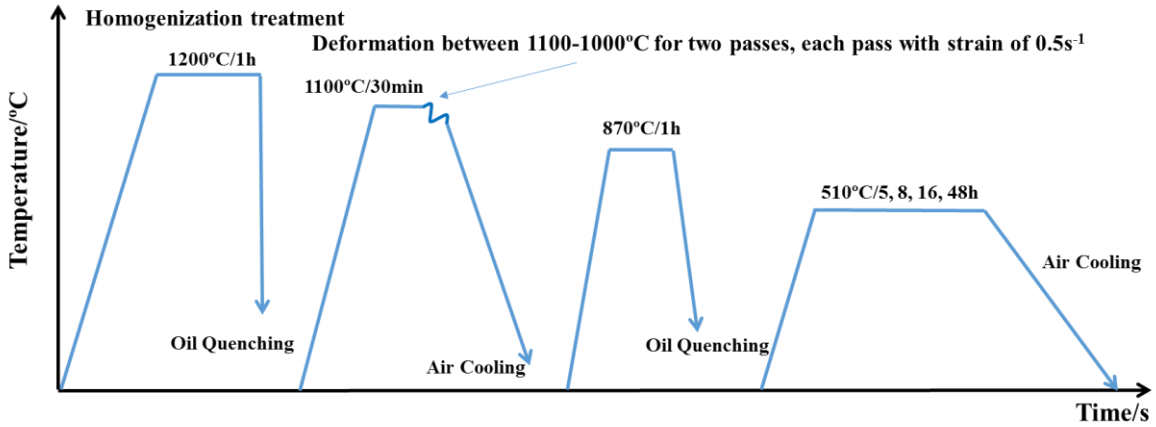

Fig. 2. Schematic of the thermomechanical cycles applied to the alloys.

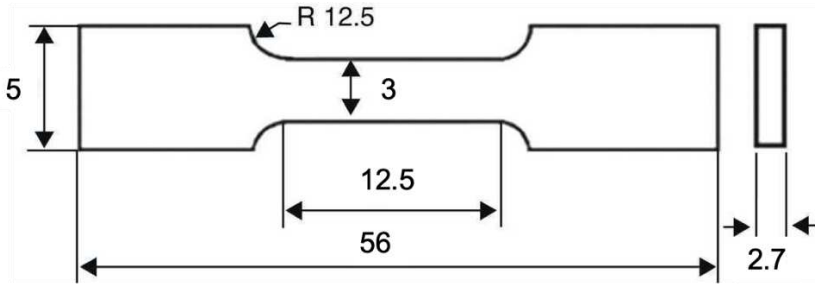

Fig. 3. Tensile sample geometry (lengths in mm).

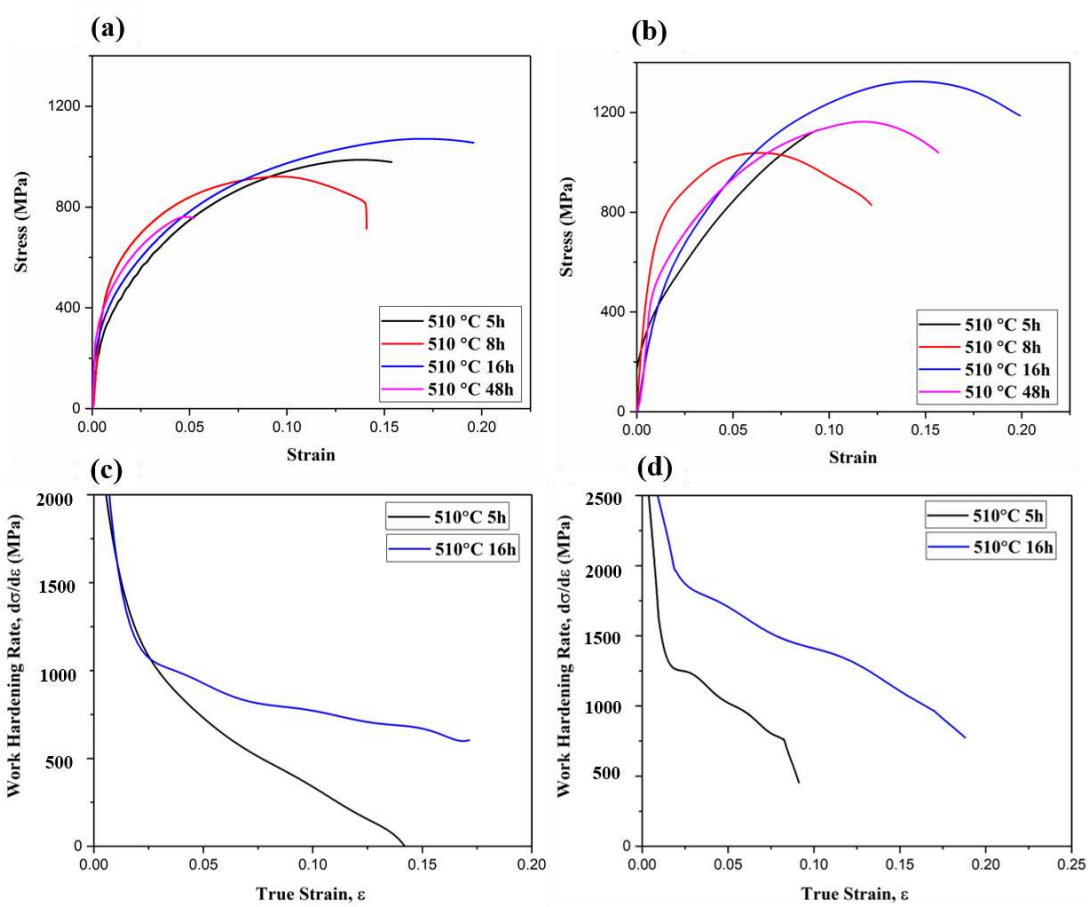

Fig. 4. The tensile test curves as a function of the ageing time at 510 °C, (a) tensile curve from 2CrMo; (b) tensile curve from Cr2Mo; (c) work hardening rate curve from 2CrMo; (d) work hardening rate curve from Cr2Mo.

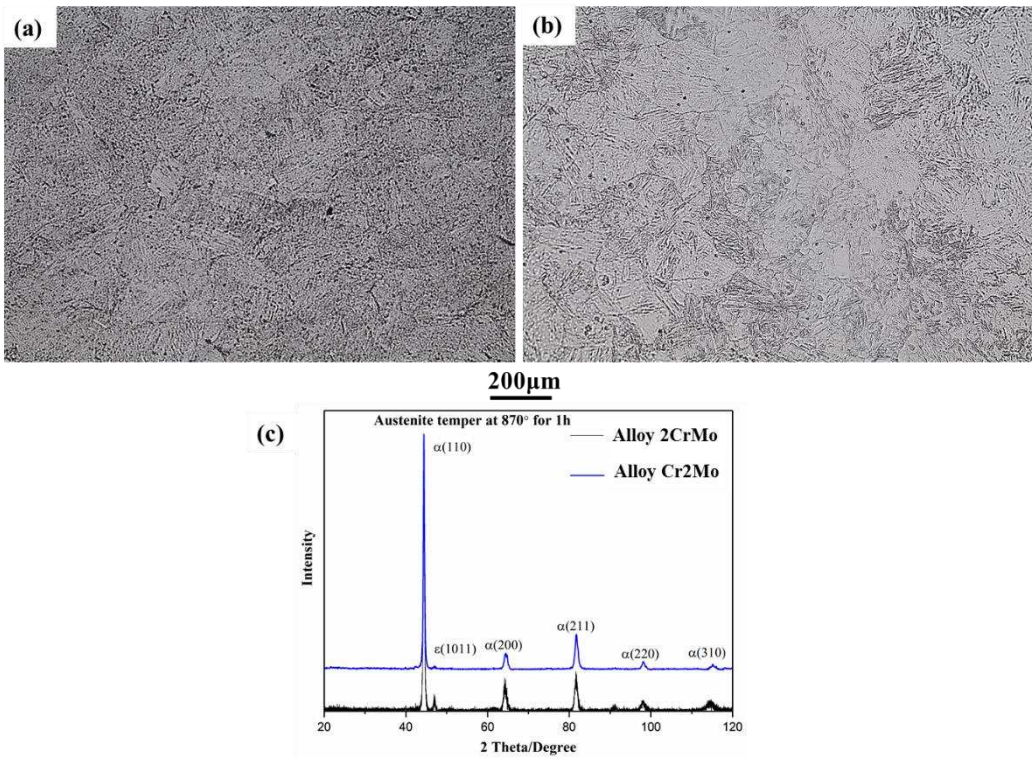

Fig. 5. Optical micrographs and XRD phase analysis of the two steels with austenitized treatment at 870 °C for 1h, (a) alloy 2CrMo; (b) alloy Cr2Mo; (c) XRD of the two steels.

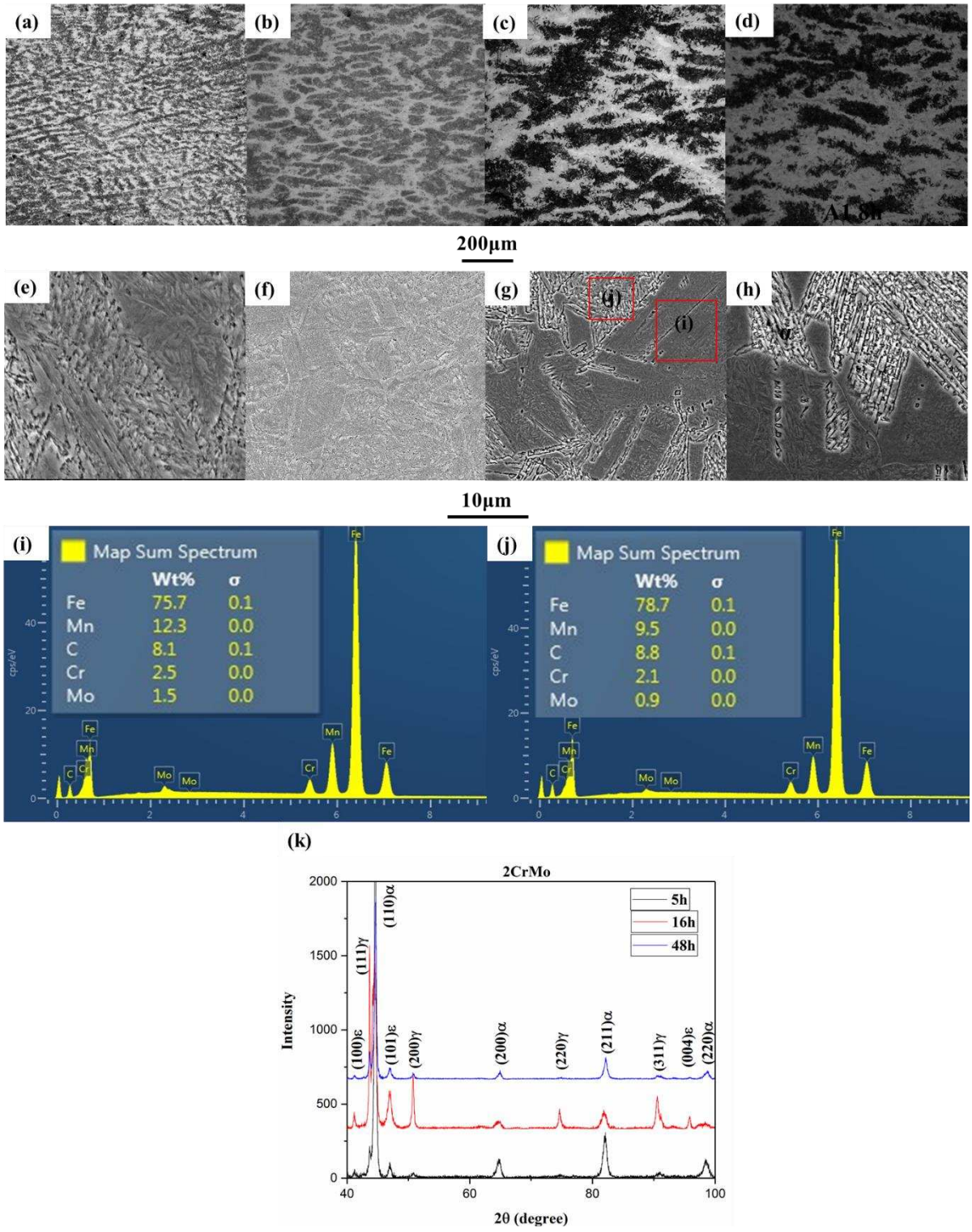

Fig. 6. Micrographs of the maraging 2CrMo steel, etched in 2% nital. (a) OM at 510 °C for 5h; (b) OM at 510 °C for 8h; (c) OM at 510 °C for 16h; (d) OM at 510 °C for 48h; (e) SEM at 510 °C for 5h; (f) SEM at 510 °C for 8h; (g) SEM at 510°C for 16h; (h) SEM at 510 °C for 48h; (i) EDS spectrum from region labelled (i) from the α'_F in (g). Note carbon level is artificially high through carbon contamination; (j) EDS spectrum from region labelled (j) from the α'_T in (g). Note carbon level is artificially high through carbon contamination; (k) XRD for different heat treatment times for 2CrMo.

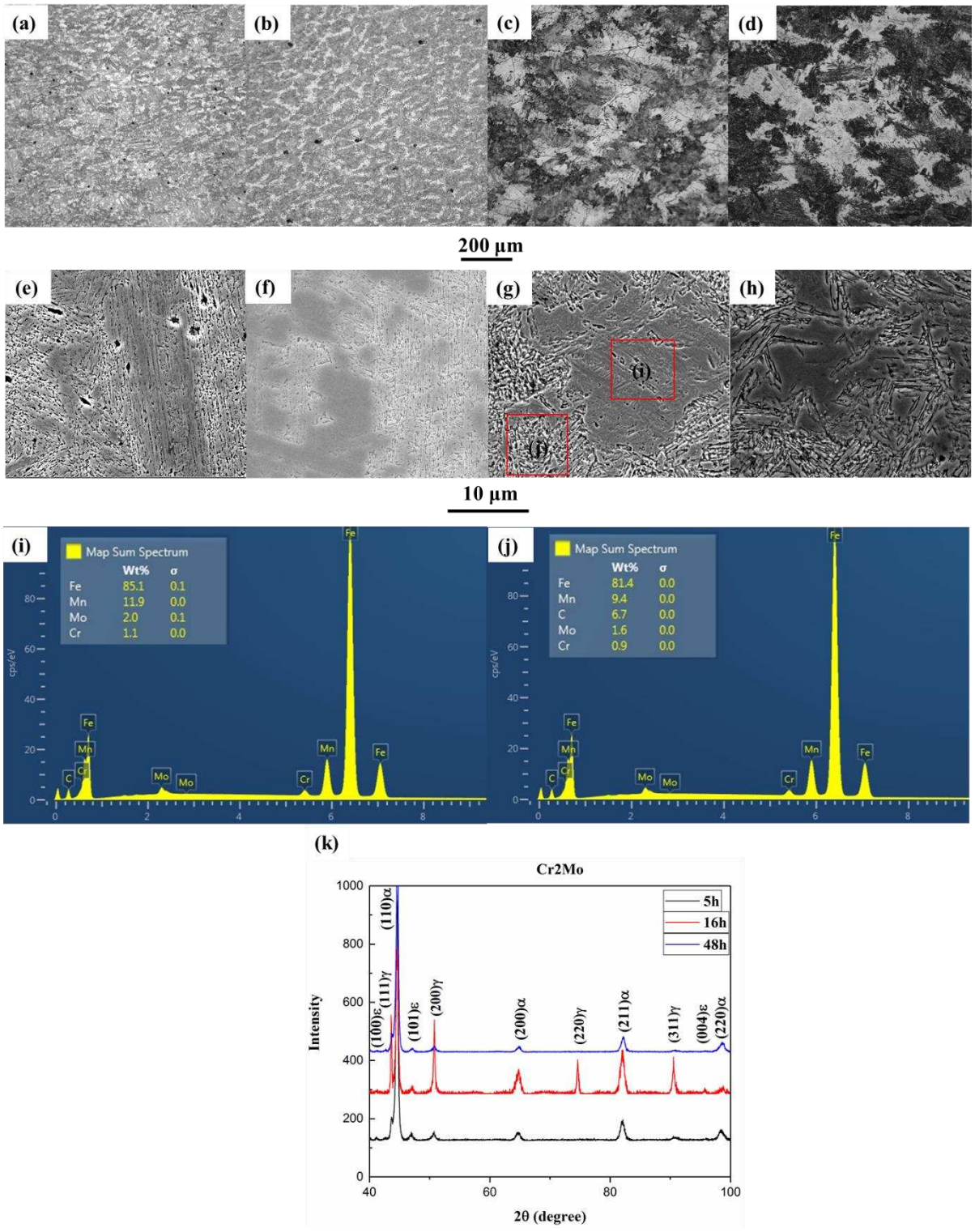

Fig. 7. Micrographs of the Cr2Mo steel, etched in 2% nital. (a) OM at 510 °C for 5h; (b) OM at 510 °C for 8h; (c) OM at 510 °C for 16h; (d) OM at 510 °C for 48h; (e) SEM at 510 °C for 5h; (f) SEM at 510 °C for 8h; (g) SEM at 510°C for 16h; (h) SEM at 510 °C for 48h; (i) EDS spectrum from region labelled (i) from α'_F in (g). Note carbon level is artificially high through carbon contamination; (j) EDS spectrum from region labelled (j) from α'_T in (g). Note carbon level is artificially high through carbon contamination; (k) XRD for different heat treatment times for 2CrMo.

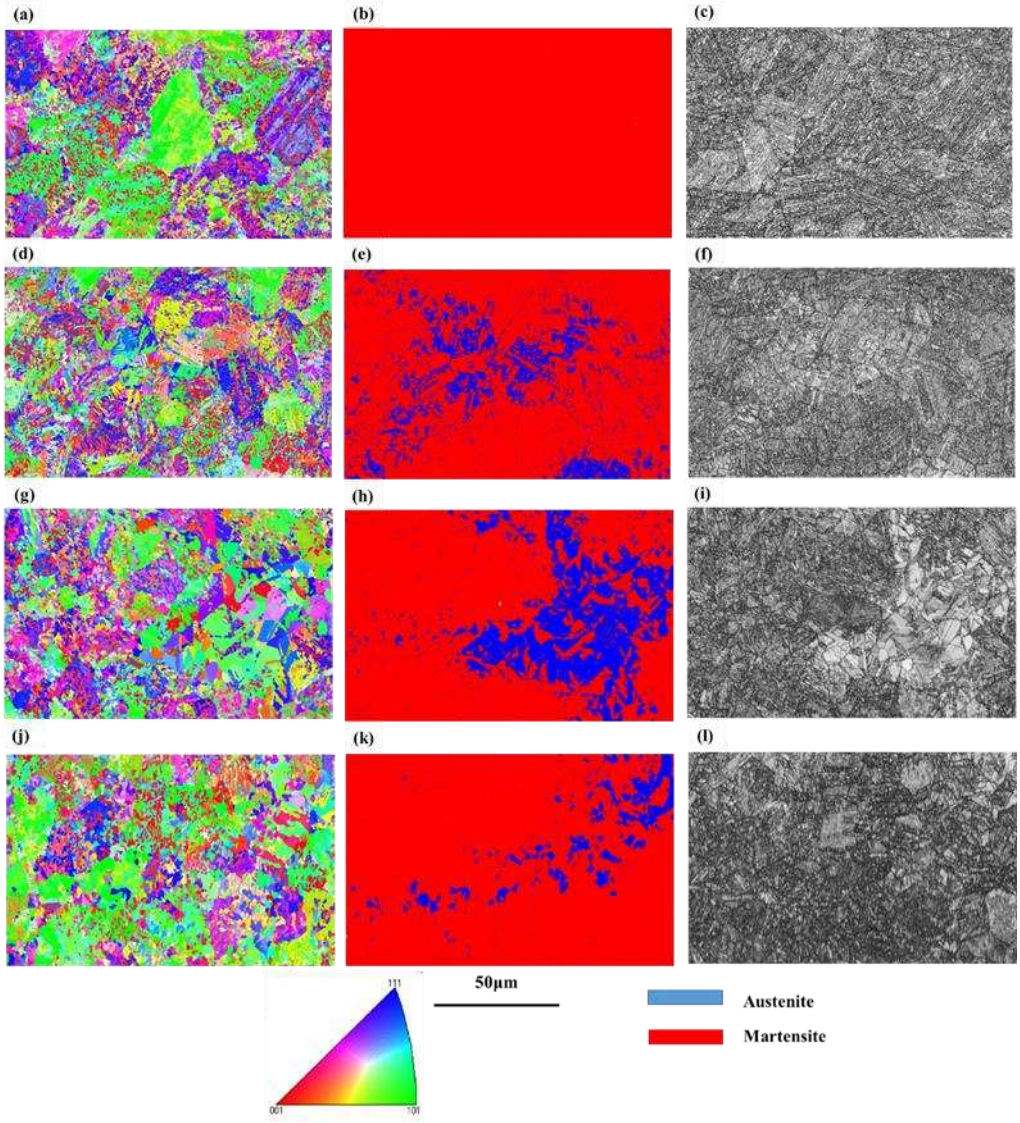

Fig. 8. EBSD maps of 2CrMo showing the aged microstructure evolution from (a-c) 510 °C for 5h; (d-f) 510 °C for 8h; (g-i) 510 °C for 16h; (j-l) 510 °C for 48h. Inverse pole figures (IPF) maps (a,d,g,j) show the grain orientations with respect to RD (rolling direction); (b,e,h,k) phase maps with blue for FCC reverted austenite and red for martensite; (c,f,i,l) Band Contrast maps showing the morphology of the two phases.

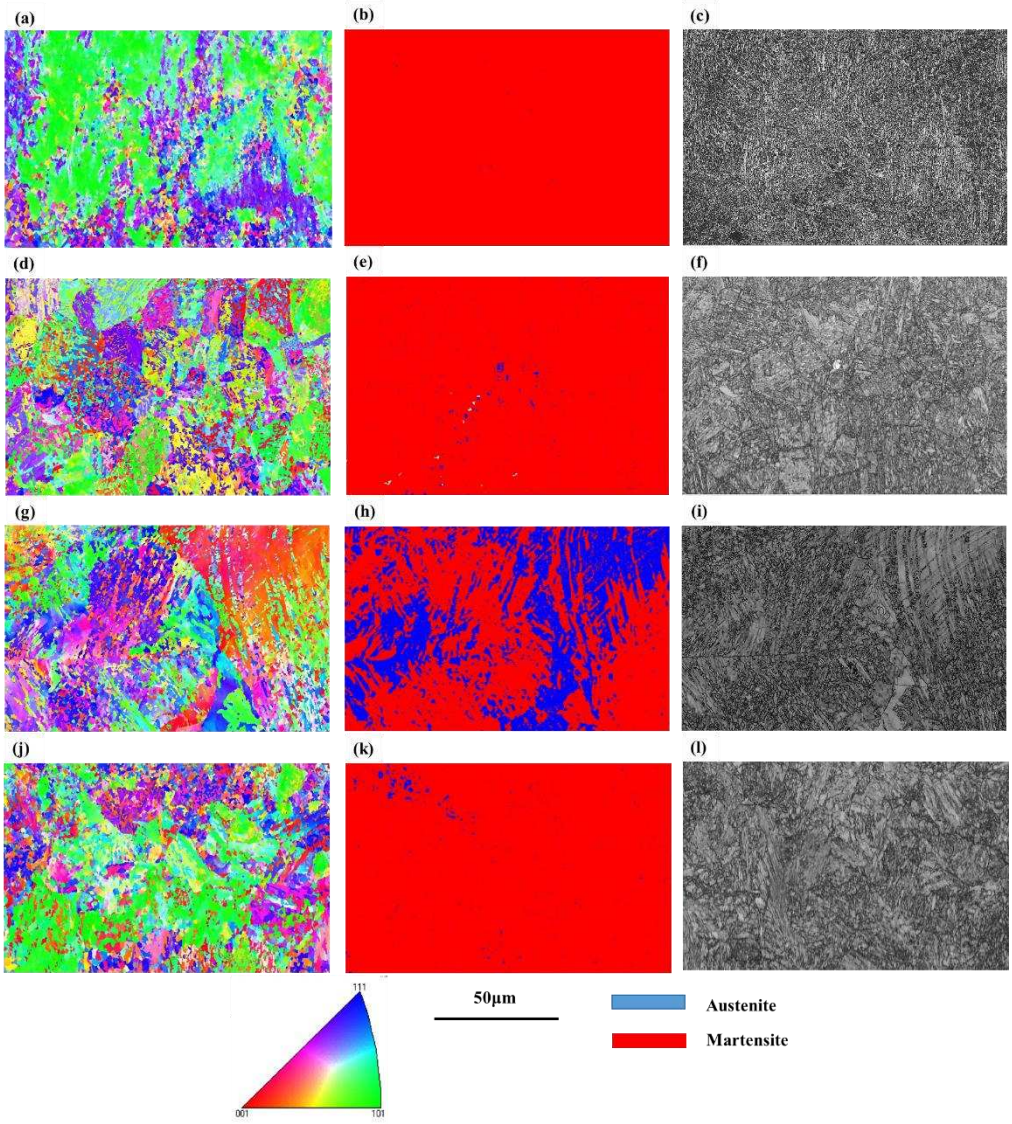

Fig. 9. EBSD maps of Cr2Mo showing the aged microstructure evolution from (a-c) 510 °C for 5h; (d-f) 510 °C for 8h; (g-i) 510 °C for 16h; (j-l) 510 °C for 48h. Inverse pole figures (IPF) maps (a,d,g,j) show the grain orientations with respect to RD (rolling direction); (b,e,h,k) phase maps with blue for FCC reverted austenite and red for martensite; (c,f,i,l) Band Contrast maps showing the morphology of the two phases.

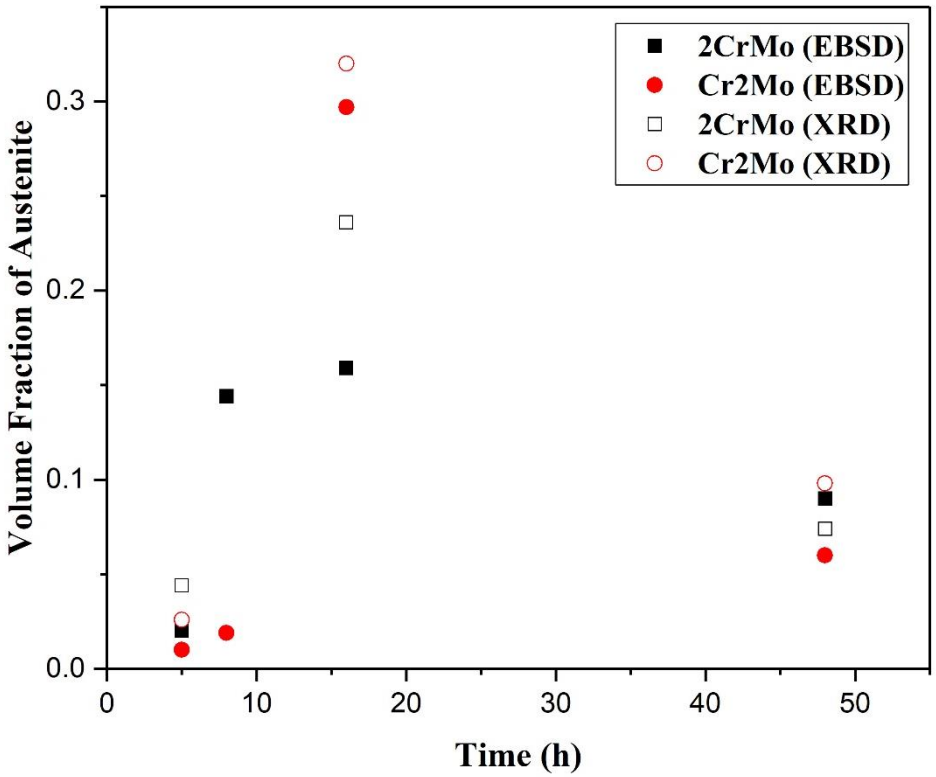

Fig. 10. The volume fraction of austenite in 2CrMo and Cr2Mo. The data from EBSD results with the specimens were annealed 5h, 8h, 16h and 48h at 510°C; the data from XRD results with the specimens were annealed 5h, 16h and 48h at 510°C.

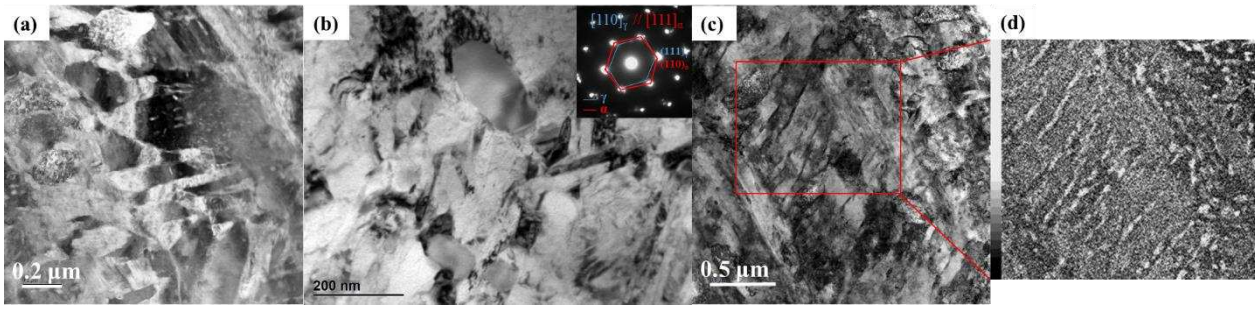

Fig. 11. TEM and STEM micrographs on the 2CrMo after ageing for 5h: (a) STEM dark field image of two types of martensite (α'_T and α'_F) with carbides in the α'_T; (b) TEM image of reverted austenite in the martensite with corresponding select area electron diffraction (SAED) pattern. The reverted austenite has a mid-grey contrast and is featureless, suggesting it is globular austenite; (c) STEM high angle annular dark field image showing the tempered martensite with nanoscale carbides (d) corresponding EDS map showing the Mn distribution on lath martensite region from (c).

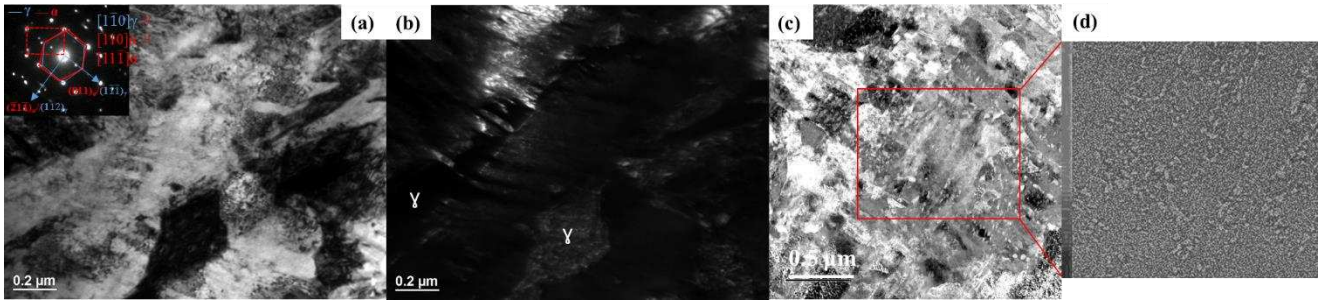

Fig. 12. TEM and STEM micrographs taken from 2CrMo after ageing for 8h: (a) TEM bright field image of reverted austenite in α'_T martensite phase with the corresponding SAED pattern; (b) TEM dark field image with $g=(011)_\alpha//(011)_\gamma$ from (a) shown the reverted austenite formed on the lath martensite boundaries; (c) STEM-dark field image in the α'_T martensite showing carbides and some reverted austenite particles on the lath grain boundaries and (d) STEM-EDS Mn map showing the carbides in (c).

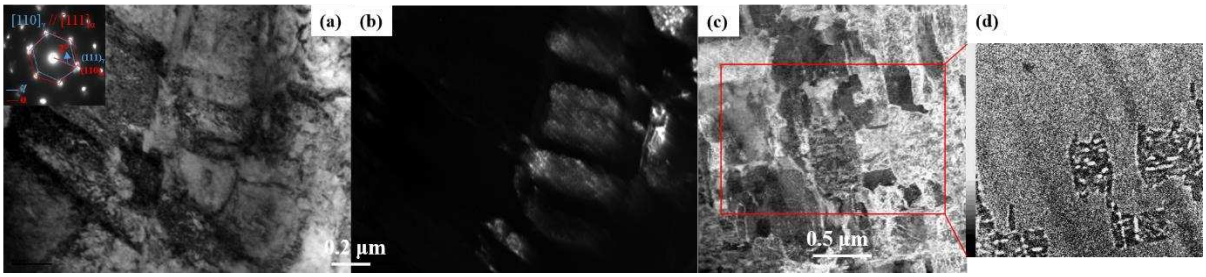

Fig. 13. TEM and STEM micrographs taken from 2CrMo after ageing for 16 h: (a) TEM bright field image of reverted austenite in α'_T martensite phase with the corresponding SAED pattern; (b) TEM dark field image with $g=(011)_\gamma$ from (a) shown the reverted austenite; (c) STEM-dark field image of the austenite and tempered martensite and (d) EDS Mn map shown the carbides in corresponding image (c).

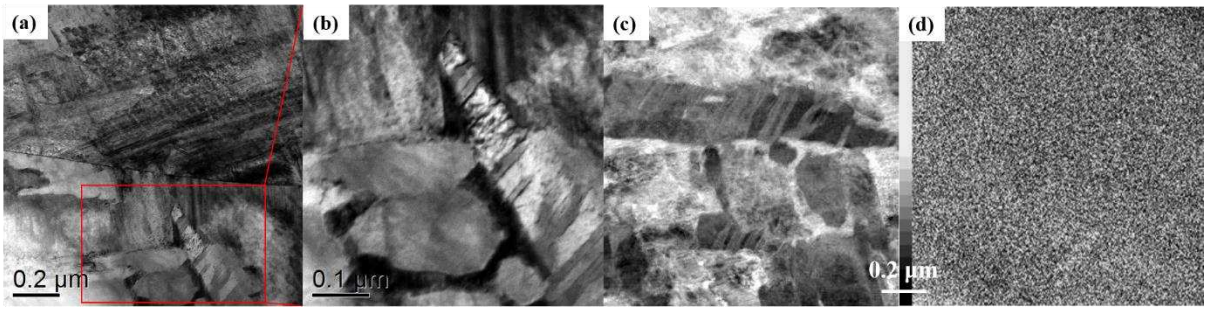

Fig. 14. STEM micrographs taken from 2CrMo after ageing for 48 h: (a) the STEM bright field image of tempered martensite (α'_T) and fresh martensite (α'_F); (b) higher magnification from the region marked in the red square showing the reverted austenite with partially transformed to fresh twinned martensite; (c) STEM-dark field image of fresh martensite, α'_F and (d) STEM EDS Mn mapping corresponding to image (c).

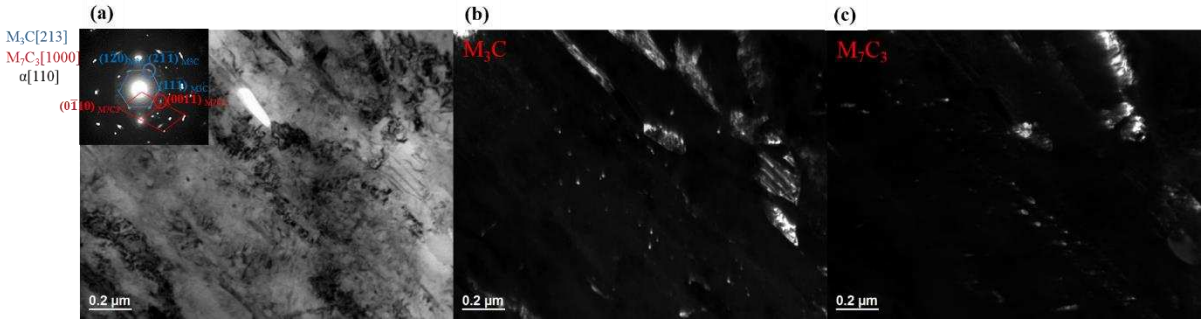

Fig. 15. Micrographs of carbide precipitates in 2CrMo steel after ageing for 8h: (a) the bright field image with its corresponding SAED pattern; (b) the dark field image of M_3C carbides takes with g=$(2\bar{1}\bar{1})_{M3C}$ from (a); (c) dark field of carbides taken with g=$(001\bar{1})_{M7C3}$ from (a).

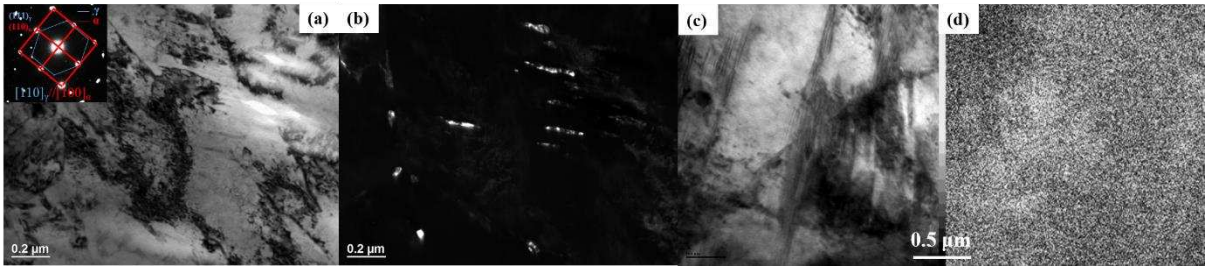

Figure 16. TEM and STEM micrographs taken from Cr2Mo after ageing for 5h: (a) TEM bright field image from α ′$_T$ martensite with corresponding SAED pattern; (b) TEM dark field with g=$(011)_\gamma$ from (a) shown the reverted austenite sited on the martenite lath boundaries; (c) STEM-dark field image from α′$_S$ martensite; (d) STEM EDS Mn map corresponding to image (c).

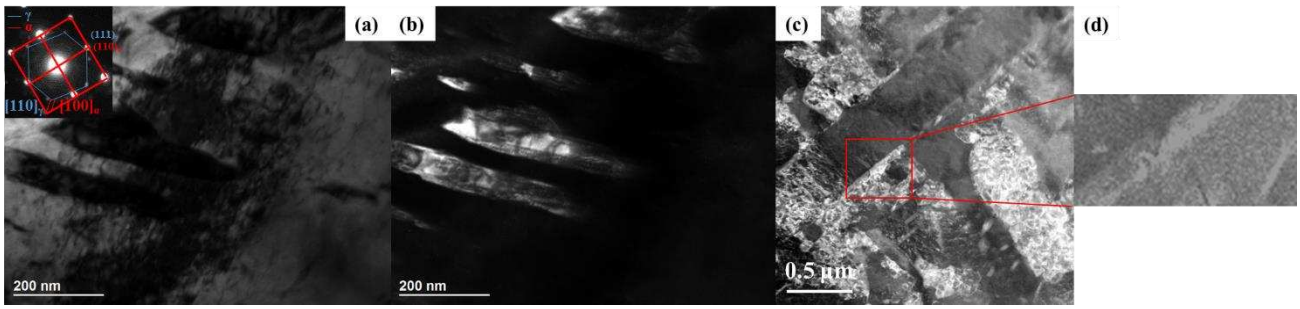

Figure 17. TEM and STEM micrographs taken from Cr2Mo after ageing for 8 h: (a) TEM bright field image from α′$_T$ martensite with corresponding SAED pattern; (b) TEM dark field with g=$(011)_\gamma$ from (a) showing the reverted austenite growth along the martenite lath boundaries; (c) STEM-dark field image from α ′$_T$ martensite phase with martensite boundaries; (d) STEM EDS Mn mapping corresponding to image (c) showing Mn segregation with no carbides on the boundaries.

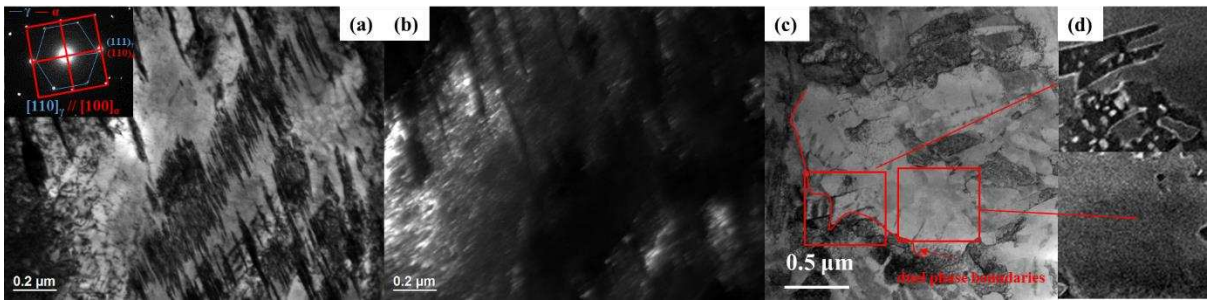

Fig. 18. TEM and STEM micrographs taken from Cr2Mo after ageing for 16 h: (a) TEM bright field image with corresponding SAED pattern from α ′T martensite and reverted austenite; (b) TEM dark field with g=(011)γ from (a) showing the reverted austenite; (c) STEM-bright field image from α′T martensite with partially transformed to reverted austenite; (d) STEM EDS Mn mapping corresponding to image (c) showing carbides and Mn segregation at the austenite/martensite phase boundaries region and homogenous composition in the reverted austenite phase region.

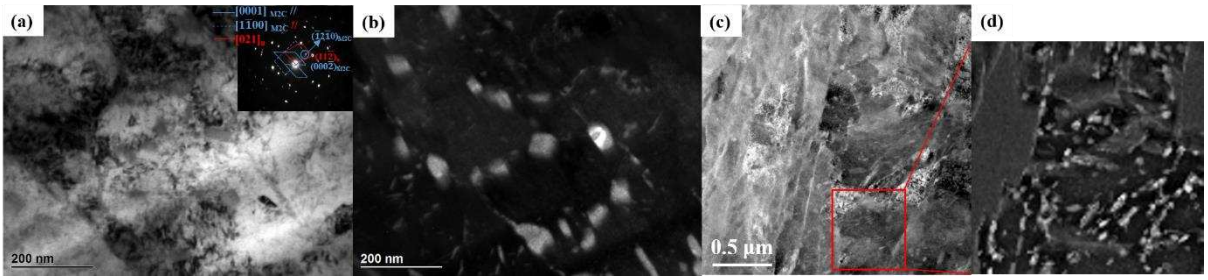

Fig. 19. TEM and STEM micrographs taken from Cr2Mo after ageing for 48 h: (a) TEM bright field image of fresh martensite with its corresponding SAED pattern; (b) TEM dark field image with g=$(\bar{1}2\bar{1}0)_{M2C}$ from (a) showing large carbides on the grain boundaries and small carbides within the grains; (c) STEM-bright field image from fresh martensite; (d) STEM EDS Mn map corresponding to image (c) showing carbides formed in the region.

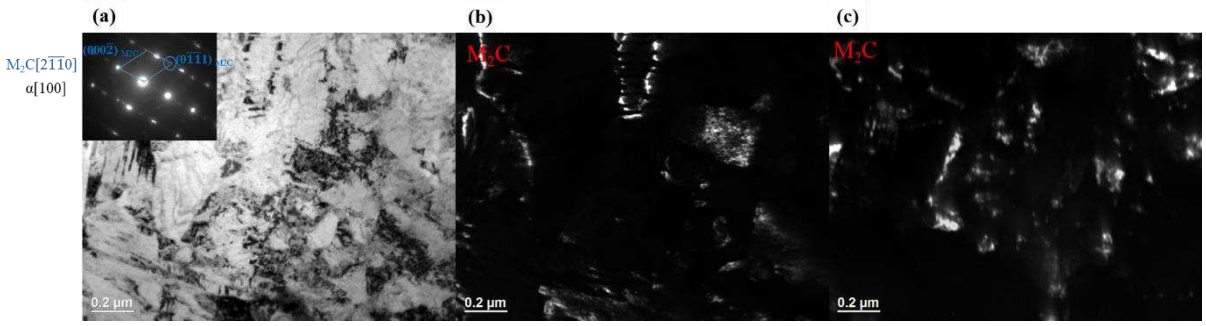

Fig. 20. Carbide precipitation in the tempered martensite in Cr2Mo aged for 16 hours. (a) TEM bright field image with its corresponding SAED pattern; (b) TEM dark field image of M_2C precipitates taken with g=$(0\bar{1}\bar{1}0)_{M2C}$ from (a) diffraction pattern; (c) TEM dark field of M_2C precipitates in the grains taken with g=$(000\bar{2})_{M2C}$ from (a) diffraction pattern.

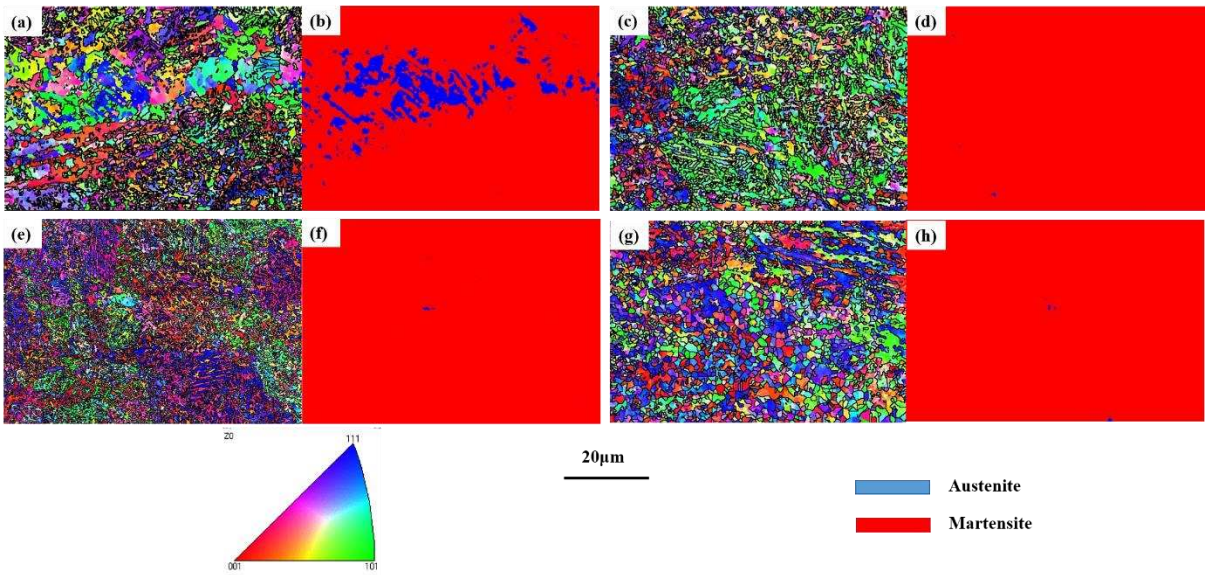

Fig. 21. EBSD maps of the specimens aged for 8h (a-d) and 16h (a-d) after tensile testing: (a, b) 2CrMo showing some austenite retention after the tensile test; (c, d) Cr2Mo showing virtually no austenite after the tensile test; (e, f) 2CrMo showing virtually no austenite after the tensile test; (g, h) Cr2Mo showing virtually no austenite after the tensile test. (a, c) are IPF map and (b, c) are phase maps. (IPF: inverse pole figure; phase map: blue-reverted austenite, red-martenite).

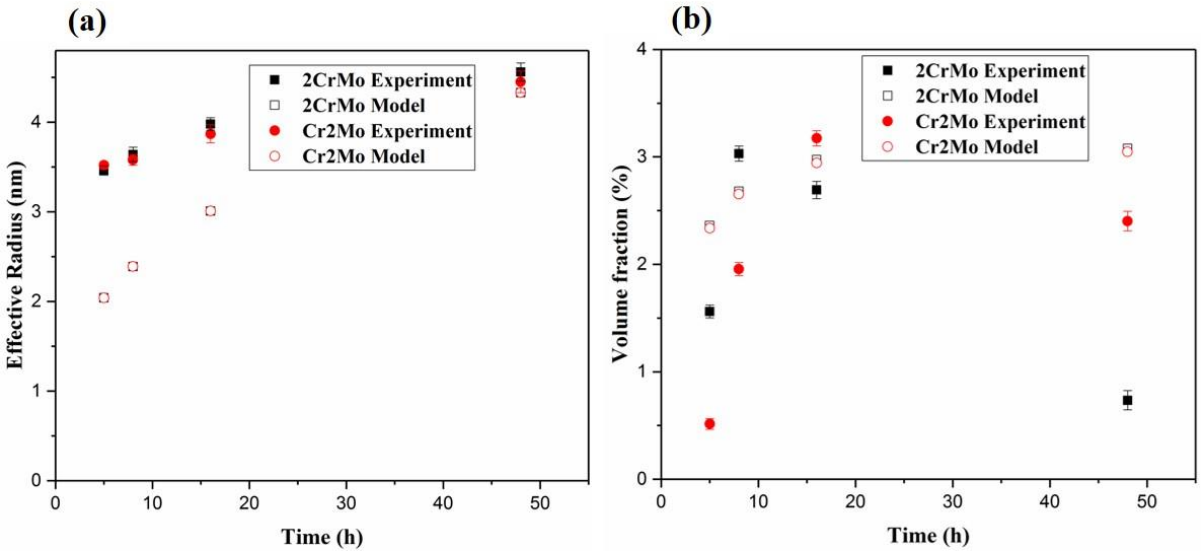

Fig. 22. Predicted and measured carbide (a) effective radius and (b) volume fraction in 2CrMo and Cr2Mo.

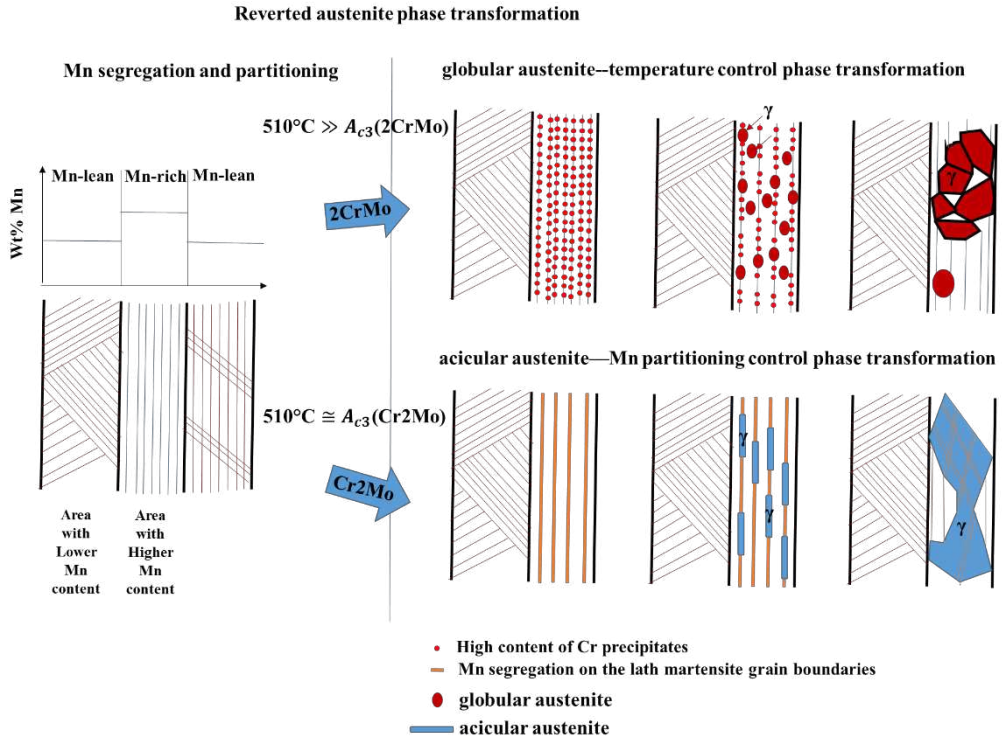

Fig. 23. Schematic of the microstructural evolution, showing carbide precipitation, Mn segregation and the location and morphology of the reverted austenite for the two steels.